
# UNIVERSITA' DEGLI STUDI DI NAPOLI "FEDERICO II"

Dipartimento di Scienze Biomediche Avanzate


## DOTTORATO DI RICERCA IN SCIENZE BIOMORFOLOGICHE E CHIRURGICHE

## XXIX ciclo

*Coordinatore: Prof. Alberto Cuocolo*

# In vivo imaging of TSPO in mouse model of neuroinflammation using small-animal PET with [18F]DPA-714


Tutor:
Prof.ssa Sabina Pappatà

Dottorando:
Anna Rita Daniela Coda



Academic Year 2015-2016

# Contents

# 1. Introduction

## 1.1. Neuroinflammatory processes and microglial activation

Historically the Roman Celsius is considered the first to have defined the four cardinal signs that characterized inflammation: “rubor et tumor cum calore et dolore” (redness and swelling with heat and pain). This definition of inflammation is still in use, however in recent years new models of inflammation have been developed. They are based on molecular phenomena, in fact the term “inflammation” refers to a generic multicellular process, characterized by changes in local vasculature, activation of resident immune competent cells, infiltration of mobile cells of the immune system and cytokine production *[1]*. Neuroinflammation (NI) is the inflammation of the nervous system, observed in disease of the Central Nervous System (CNS). All these neuropathologies are characterized by a series of complex events involving microglia, astrocytes and infiltrating peripheral immune cells, important in neurodegenerative processes and tissue repair *[2]*. NI typically occurs when blood–brain barrier (BBB) is not able to stop biological insults, but it may also occur in acute noninfectious neuropathologies like stroke or chronic diseases such as multiple sclerosis, neurodegenerative and psychiatric disorders *[3]*. Acute lesions usually induce an important neuroinflammatory response leading to local changes of blood flow and vascular permeability, alteration of the BBB, infiltration of peripheral macrophages and activation of resident microglia *[4]*. Moreover, the pathogenesis and

progression of chronic neurodegenerative diseases are characterized by an important inflammatory response, primarily mediated by specific cells as microglia and astrocytes *[5]*. CNS presents biological links at many levels and it is highly integrated with the immune system *[6]*. The first evidence that support the connection between CNS and immune system is the presence of hypothalamus–pituitary–adrenal (HPA) axis, an immune-neuro-endocrine circuit characterized by interconnection involving peripheral immune mechanisms and endocrine responses under brain control *[7]*. An important event is the release of regulatory signaling factors as corticosteroids and proinflammatory cytokines like tumor necrosis factor-alpha (TNF-α) and interleukin 6 (IL-6), that not only influence the HPA axis–mediated glucocorticoid feedback loop, but also they are involved in the regulation of a variety of neuronal circuits such as thermoregulation, food intake and other behaviors related to diseases. These pro-inflammatory cytokines, generated in the periphery, communicate with the brain, to initiate cytokine synthesis in the CNS *[8]*.

In fact cytokines secreted by immune cells in the periphery, cannot diffuse across an intact blood–brain barrier (BBB) although there is evidence that they can diffuse from the circulation to BBB deficient brain areas, like the choroid plexus and circumventricular organs or can be carried by endothelial cell transporter into the CNS *[9]*. Alternatively, to transmit a stimulatory signal to the CNS, blood-borne cytokines have to activate BBB endothelial cells and consequently neurons, through the involvement of soluble factors and activation of glial cells *[10]*.

Glial cells constitute a large percentage of cells in the nervous system. Glia has an active role in brain function and is involved in every type of neurodegenerative disease, in particular the main actors of the innate immune response of the CNS are microglial cells that represent approximately 10% of the entire population of the brain. Microglia are myeloid cells of the CNS that are derived from early embryonic erythro-myeloid progenitor cells and have migrated into the developing nervous tissue, where they begin the maturation process into brain-resident microglial cells. Microglia are involved in various developmental processes such as cerebral tissue homeostasis, apoptosis, axonal growth and guidance, regulation of embryonic cortical precursor, cell development, neuronal differentiation, angiogenesis, phagocytosis of extracellular debris, secretion of inflammatory mediators and production of factors important for astrocytes, another type of glial cells with support functions *[11]*. Under physiological conditions, microglia show a noninflammatory phenotype, but after various environmental and noxious stimuli, can change from a resting to an activated state. The processes of microglia activation is associated with proliferation and transformation into reactive microglia with different response phenotypes. In healthy brain, microglial cells are quiescent and non-motile cells, characterized by a small cell body with fine, branched processes and low expression of surface antigens *[12]*. Under pathological conditions such as infectious diseases, stroke or neurodegenerative processes, microglia become activated through a rapid transformation into a phagocytic state. During this transition microglial cells, with a larger cell body and shorter cellular processes, become motile and use

amoeboid-like movements, to migrate to and within the lesion site (Fig. 1).

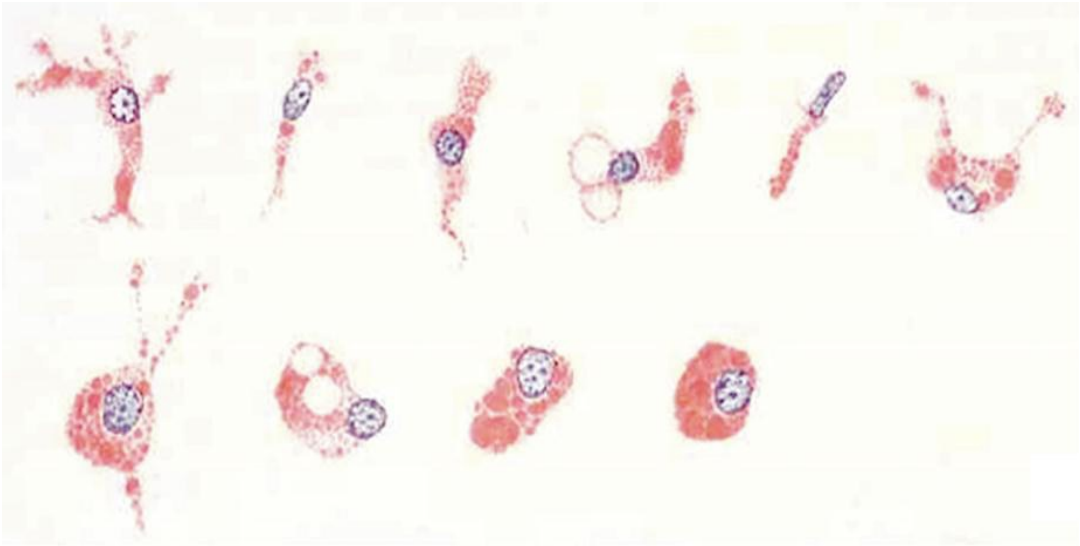

**Fig. 1.** Illustration of microglial phenotypic plasticity in CNS *(Graeber et al. 2011) [1]*.

Activated microglia not only change their phenotype and migrate to the site of damage, but also clear cellular debris by phagocytosis and release a large amounts of soluble factors that include pro- and anti-inflammatory cytokines and chemokines, oxidative stress-inducing factors like nitric oxide (NO) as well as growth factors and immunomodulatory factors and reactive oxygen species (ROS) *[13]*. In particular, the simplest manner to describe microglial activation is to use the similarity with two macrophage types described in peripheral inflammation. Depending on the mode of activation, surveying microglia may come into two phenotypes: the proinflammatory "M1" phenotype, activated by lipopolysaccharides and interferon-γ, corresponds to classical macrophage activation, while the anti-inflammatory "M2" phenotype is activated by

interleukin (IL)-4 and IL-13 through the "alternative" pathway of macrophage activation. M1-type microglia produce tumor necrosis factor-α, IL-1β, IL-6, nitric oxide, superoxide, hydrogen peroxide, and matrix metalloproteinases. The M1 microglia phenotype actively participates in host defense against pathogens and tumor cells, but also triggers damage to healthy neurons. In contrast, the anti-inflammatory M2 microglia phenotype expresses IL-10 and arginase-1 and promotes tissue remodeling/repair and angiogenesis *[13]* (Fig. 2).

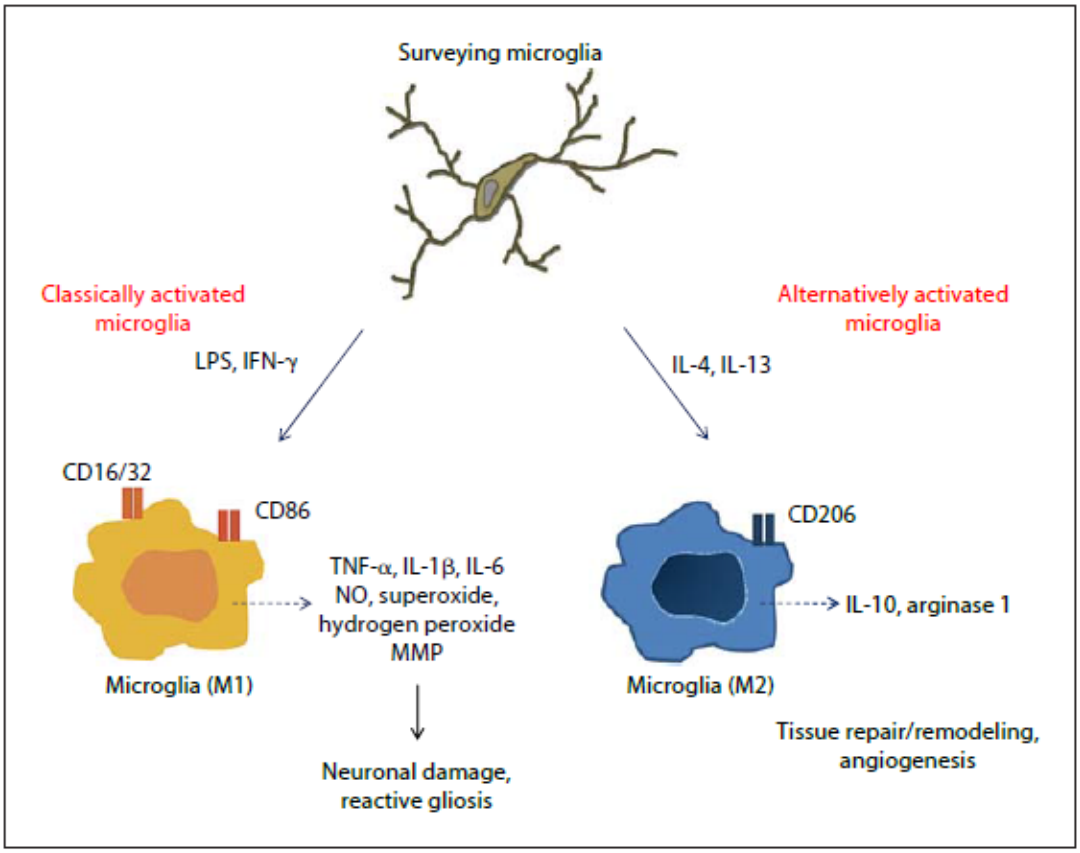


**Fig. 2.** Macrophages/microglia can be classified in a simplified manner into two subsets of phenotypes and effector functions depending on the activation pathway *(Czeh et al. 2011) [13]*.

## 1.2. Neuroinflammation in mouse model of human disease

There is important evidence in animal models that NI is involved in the most part of neurological disorders, making NI a potential target to diagnose diseases, to monitor the progression and to test new therapies *[14]*. An increasing number of interventional or transgenic rodent models (rat, mouse) of acute or chronic NI, mimicking different human neuropathologies, have become available and extensively characterized *[15-16]*.

Although none of these animal models shows all aspects of human diseases, they might provide valuable information on basic molecular processes of NI that are of crucial importance for the development of novel therapeutic strategies. In particular, laboratory mice are not expensive, easy to handle and to maintain in a research facility with respect to other animal species. If compared with man, mice show adequate morphogenetic homology, and are important surrogate models of genetic and even of non-genetic disorders. A perfect animal model, like mouse, should reflect all aspects of the human disease, as symptoms, lesions and causes of the disease. It is important to evaluate continuously the models for their match with the human disease and revaluate them in light of new findings in human patients. Therefore, the use of animal models has been proven to be a useful tool to clarify underlying molecular mechanisms of neurodegenerative disorders and to discover potential therapeutic and reparative strategies *[16]*. Among neuroinflammatory pathologies, including stroke, Alzheimer's disease and Parkinson's disease, this work focused on a mouse model of chronic degeneration in amyotrophic

lateral sclerosis (ALS) and a mouse model of acute inflammation in multiple sclerosis (MS).

### 1.2.1. Amyotrophic lateral sclerosis – SOD1 G93A mouse model

Amyotrophic lateral sclerosis (ALS) is a neurodegenerative disease, characterized by a progressive loss of motor neurons (MN) in brainstem nuclei, motor cortex and spinal cord. Degeneration of MN results in muscle weakness and spasticity, and respiratory failure, leading to death within approximately 3 – 5 years of symptom onset *[17]*. Although ALS was first described more than 140 years ago by Charcot in 1874, most major advances for a better knowledge of the pathophysiology of the disease have occurred in the last 2 decades *[18]*. Recent progresses in knowledge of various genetic mutations that causes ALS, such as mutations in superoxide dismutase 1 (SOD1), have laid the basis of the generation of a number of new rodent models of disease helping to the development of new diagnostic and therapeutic strategies. SOD1 transgenic mouse has resulted the model that best describes ALS phenotype *[19]*. Most cases of human ALS are sporadic, but approximately 20 % of familial ALS and 5 % of apparently sporadic disease are associated with the gene encoding the enzyme Cu2+/Zn2+ superoxide dismutase (SOD1) *[20]*. SOD1 is the cytosolic Cu/Zn-binding isoform of SOD that catalyzes the detoxification of superoxide radical ($O_2^-$) to convert it to hydrogen peroxide ($H_2O_2$), when there is a reduction or an increase in SOD enzyme, activity oxidative stress occurs *[21]*.

The point mutation in the gene encoding SOD1 was identified in 1993 *[22]* and since then, ALS research has advanced substantially by

studying rodent models and exploring how mutations in SOD might selectively cause motor neuron degeneration. Several SOD1 mutants of transgenic mice have been generated *[23]* and the G93A and G37R mutations are the most commonly used to generate transgenic ALS models, respectively with the substitution of arginine for glycine at position 37 and the substitution of glycine for alanine at position 93 *[24-25]*.

These mice exhibit the ALS-like clinical features that are transmitted in an autosomal dominant way *[26]*. The progressive motor neuron degeneration is characterized by hind limb weakness and tremulous movements as initial symptoms, followed by more severe symptoms such as progressive motor paralysis and disability of gait, eating and drinking, and death within some weeks. The mechanisms characterizing neurodegeneration in ALS are multifactorial and involve a complex interaction between molecular and genetic pathways. Neuroinflammation and activated microglia are neuropathological features of ALS and play a significant role in MN degeneration and disease progression *[27]*. Studies on human ex-vivo tissues have shown astrocytosis and microgliosis in motor cortex, motor nuclei of the brainstem, anterior horn of the spinal cord, and corticospinal tract *[28]*. Interestingly, the transgenic mouse overexpressing a mutant form of human SOD1, also displays ex-vivo similar inflammatory responses to those seen in ALS patients, including activated microglia, astrogliosis and infiltrating lymphocytes also with MN injury in brainstem and spinal cord *[29]*. Therefore, mouse models of ALS, like SOD1-G93A, is a good model that give a useful and relevant tool for investigating neuroinflammation.

### 1.2.2. Experimental autoimmune encephalomyelitis – EAE mouse model

Multiple sclerosis (MS) is an autoimmune, neuroinflammatory and neurodegenerative disease of CNS. The pathological hallmarks are focal demyelinated plaques within the CNS showing different degree of inflammation, gliosis and axonal damage depending the timing and clinical phenotype *[2]*. Although MS is primarily a disease affecting the white matter, recent studies suggest that demyelinated lesions might be found in the cortical gray matter of MS patients *[30]*. The NI response in MS is mediated by peripheral lymphocytes and activated monocytes and as well as by innate immune cells, in particular microglia may contribute both to degeneration and, as recently suggested, to tissue repair *[31]*. The sclerotic plaques are characterized by an inflammatory reaction involving T cells, B cells and extensive macrophage/microglia activation, demyelination, remyelination and a concomitant neuronal and axonal degeneration *[32]*. Migration of aggressive myelin-reactive T cells into the CNS is followed by microglia activation and macrophage invasion with consequent oligodendrocyte destruction. Damage to oligodendrocytes leads eventually to damage of myelin sheaths, due to lack of myelin repair. The breakdown of myelin sheaths initiates a more severe wave of T-cell infiltration, which is accompanied by B-cells infiltration *[33]*. Acute lesions are characterized by inflammatory cell infiltration, myelin sheath debris and BBB damage, instead chronic lesions present low levels of inflammation and absence of active myelin breakdown *[34-35]*. Experimental autoimmune encephalomyelitis (EAE) is the most commonly used preclinical model that reproduces the key

pathological features of human MS *[36]* and is the most widely studied in the research field. The origins of this animal model go back to the 1920s, when an inflammation in rabbits spinal cord was induced by inoculation with human spinal cord *[37]*. After that, one of the first experiment was studied in the 1930s, when monkeys were immunized with repeated injections of rabbit brain extracts *[38]* and afterwards with the addition of Freund's adjuvant *[39]*. Only some years later**,** the immunization was complemented by pertussis toxin *[40]*. Although EAE model has been induced in various animal species, rodents are the most extensively used in biomedical research, and in the last decades, they have been widely characterized, using different strains to reproduce MS after immunization with myelin proteins or peptides *[41]*. The most relevant immunogens are derived from self-CNS proteins or peptides, usually parenteral administered in adjuvants such as complete Freund's adjuvant and pertussis toxin.

Depending of the immunizing neuroantigen and the rodent strain used, different clinical phenotypes of MS and histological/ neuroinflammatory changes can be obtained: proteolipid protein peptide ($PLP_{139-151}$) induced a relapsing remitting disease course in SJL mice; myelin basic protein (MBP) induced a non-demyelinating acute monophasic disease in PL/J mice; chronic-progressive models of myelin oligodendrocyte glycoprotein ($MOG_{35-55}$) peptide induced disease in C57/BL6 mice *[36]*.

Stereotactic intrastriatal injection of heat-killed bacillus Calmette-Guérin (BCG) and subsequent activation using an intradermal injection of BCG in Lewis rat induced a chronic focal EAE *[42]*. In addition, toxin-induced EAE (cuprizone and lysophospho-lecithin)

and intracerebral virus inoculation–induced EAE are other available mouse models of MS *[43]*.

Clinical signs of rodents EAE models are characterized by a weight loss accompanied by an ascending paralysis starting from the tail and hind legs. Many factors can influence the onset and progression of disease, as age, gender, season at immunization *[44]*, genetics factor *[45]* and type of antigen *[47]*.The EAE model used for this study is characterized by immunization with $PLP_{139-151}$ peptide in complete Freund's adjuvant in SJL female mice. This model develops first symptoms between 11-12 days after immunization followed by a complete or partial recovery within 7-10 days. EAE animals showed a progressive paralysis starting from caudal to rostral areas of CNS.

## 1.3. Translocator protein TSPO and its role in neuroinflammation

The peripheral-type benzodiazepine receptor (PBR) was identified in 1977, when diazepam-binding sites were characterized in peripheral tissues. So the expression "peripheral type" benzodiazepine receptors allowed to distinguish them from the central benzodiazepine receptor, which is part of the $GABA_A$ receptor complex. Although the name PBR is widely accepted in the scientific community, in 2006 Papadopoulos and colleagues reached a consensus on a new name: translocator protein (18 kDa) (TSPO), which applies to the protein regardless of its localization *[47]*. TSPO is a component of the mitochondrial permeability transition pore (MPTP) a multimeric 140-200-kDa proteic complex that consists of different protein: the 32 kDa voltage-dependent anion channel (VDAC) and the 30-kDa adenine

nucleotide transporter (ANT). The 18-kDa protein, with five transmembrane domains, facilitates the passage of lipophilic molecules across the cellular intermembrane space. There are two other TSPO associated proteins, PBR-associated protein 1 (PRAX-1) and PBR and protein kinase A associated protein 7 (PAP7) that facilitate complex formation *[48]* (Fig. 3).

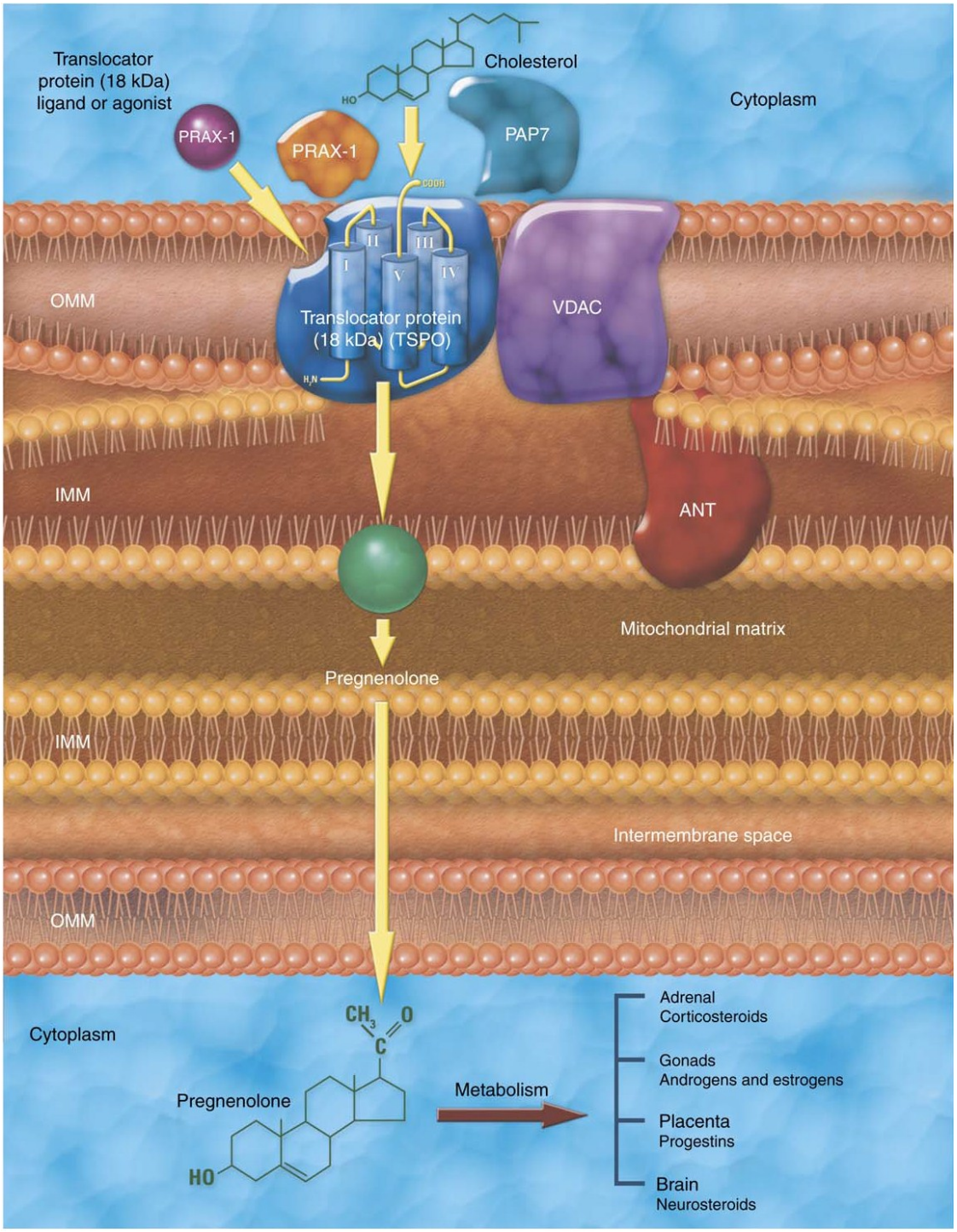


**Fig. 3.** Structure and role of TSPO for cholesterol transport into mitochondria. TSPO interacts with VDAC and ANT to form a complex that is located preferentially in outer-inner mitochondrial membrane contact sites. The TSPO-associated proteins PRAX-1 and PAP7 could facilitate complex formation or cholesterol targeting to TSPO *(Papadopoulos et al. 2006) [47]*.

TSPO participates in a lot of cellular function as cholesterol binding followed by cholesterol transport, important in steroid biosynthesis; protein import, fundamental for membrane biogenesis; porphyrin binding and transport, which is involved in heme biosynthesis, but also permeability transition pore opening, regulation of mitochondrial function, cell proliferation, differentiation and apoptosis. TSPO is widely expressed in many peripheral tissues, such as adrenals, kidneys, lung and spleen. It is also found in other region including heart, liver, testis, blood cells. Under normal condition, TSPO is expressed at very low levels in the brain, where is mainly localized in glial cells, including astrocytes and infiltrating macrophages, and at low levels in neurons. In contrast, TSPO expression increases following a neuroinflammatory event and a neuronal injury, as stroke, Parkinson's disease, Alzheimer's disease, multiple sclerosis, Huntington's disease and amyotrophic lateral sclerosis *[49]*.

The high level of TSPO expression in glial cells as well as the increased proliferation of microglia in gliosis, suggests that the expression of TSPO could serve as a marker to monitor the state and progression of brain NI following brain injury *[50-51]* (Fig 4). Interestingly, TSPO might also be a therapeutical target: modulation of TSPO expression might be also implicated in neuronal survival and regeneration *[52]*.

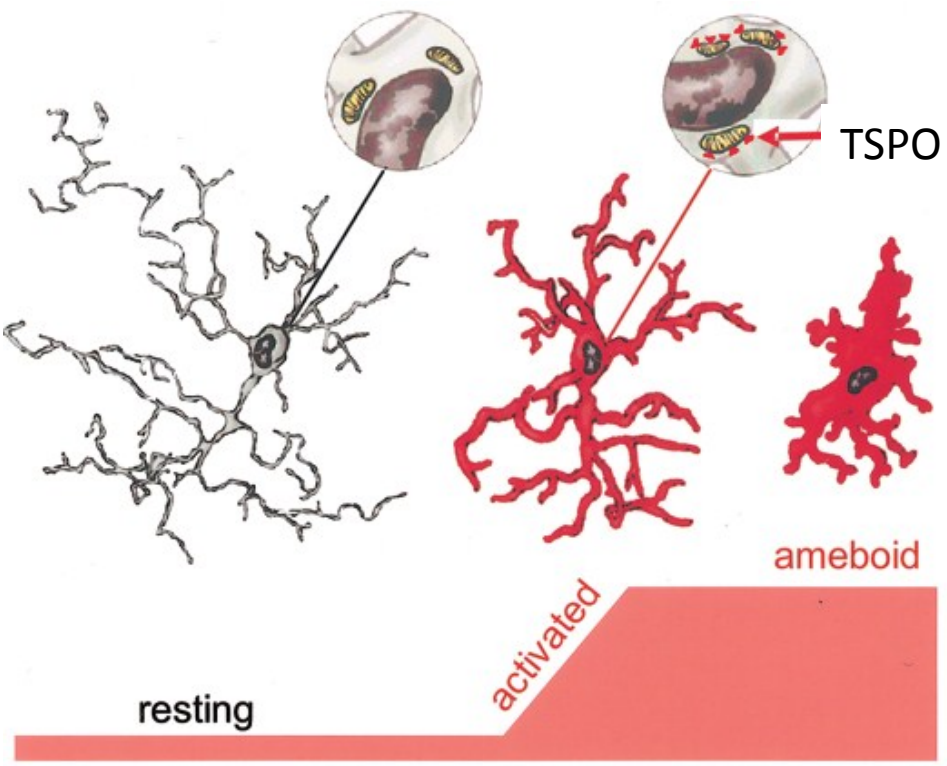


**Fig. 4.** TSPO are overexpressed by activated microglia *(Banati et al. 2002) [51]*.

## 1.4. PET and TSPO in animal models

Molecular imaging (MI) using Positron Emission Tomography (PET) may be a useful tool for in vivo study of NI in animal models. The combined use of NI rodent models and microPET is an emerging approach that contributes to the characterization and validation of new radioligands especially when combined with immunohistochemistry, allowing complementary characterization of histopathological changes underlying in vivo imaging. In additions, it allows the monitoring of the spatio-temporal dynamic of the neuroinflammatory changes occurring in neurological disorders since the earliest/asymptomatic stages, the evaluation of their relationship with disease progression

and the investigation of the effects of potential treatments. Activated microglia and astrocytes are of particular interest for radiolabeled PET probes, because they represent the innate CNS-resident immune cells, are involved in both neuroprotective and neurodegenerative processes following brain damage and are potential target for new anti-inflammatory therapies. In recent years, there has been an increase effort in the development of radioligands targeting TSPO for in vivo PET imaging of glial activation in human and animal studies *[53]*.

### 1.4.1. Principles of PET/CT

Positron emission tomography (PET) is a sensitive and specific medical technique for imaging molecular pathways in vivo and in a non-invasive way. It is based on the administration of compounds labeled with short-lived positron-emitting radionuclides. Typical isotopes used as radionuclides in PET are fluorine-18, carbon-11, nitrogen-13 and oxygen-15. These radionuclides are incorporated into biological compounds that play a specific role in different living organs. The spontaneous decay of a positron emitter produces a positron, which travels a short distance to finally react with one electron of a surrounding atom. This process is called annihilation; as a result, two gamma photons are emitted (511 keV each, emitted at 180º C to each other). The generation of these gamma rays is the basis of positron emission tomography. When a tracer containing a positron emitter is administered to an organism, the high-energy gamma rays produced, which have a high penetration power, escape from the body and are detected by an external ring of detectors as a coincident event.

The detection of hundreds of thousands of such coincident events permits the reconstruction of an image that contains information about the distribution of the radiolabeled tracer within the organism *[54]*. Integrated PET with CT in a single unit provides complementary informations and allows fusing of the anatomical data of CT with the functional information of PET (Fig. 5).

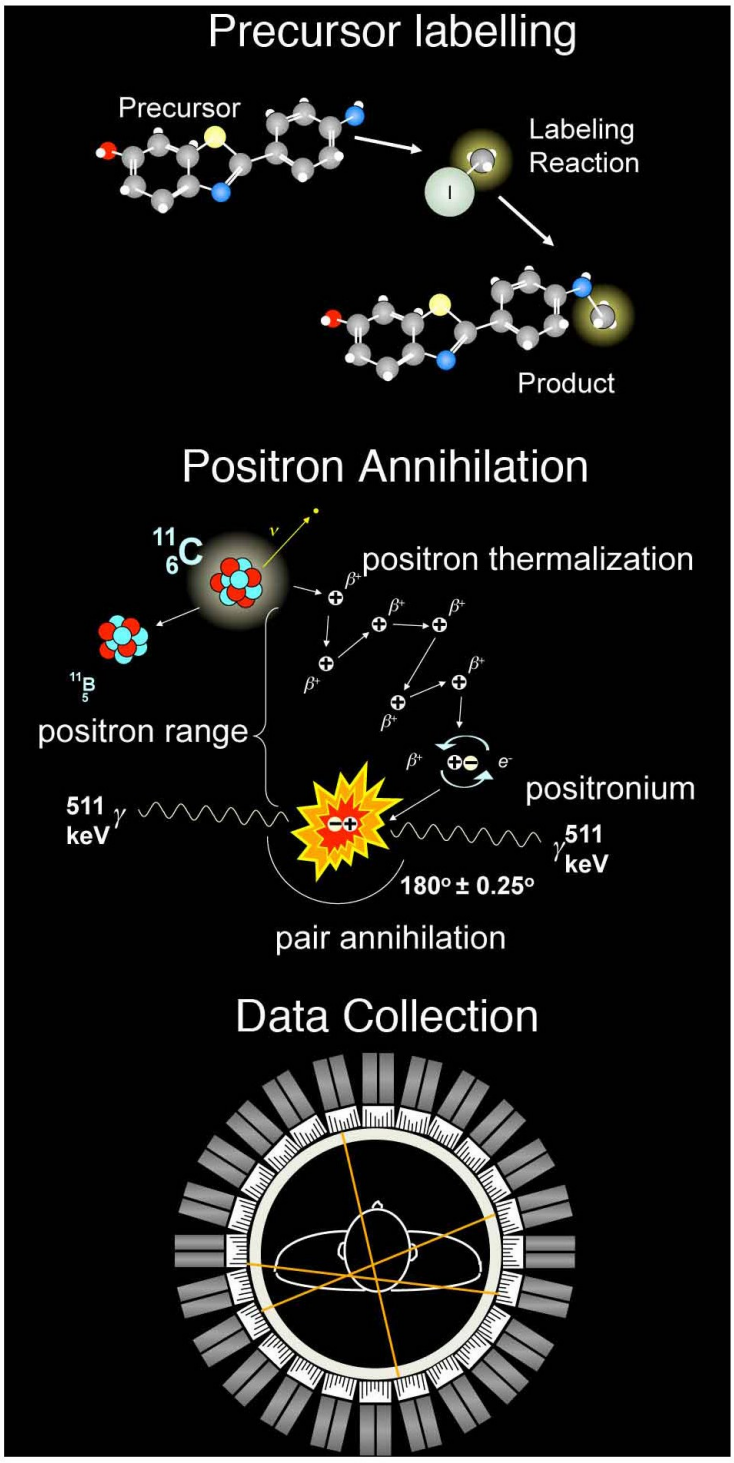


**Fig 5**. Principles of Positron Emission Tomography (Venneti et al, 2013)

### 1.4.2. TSPO PET radioligands

PK11195 [1-(2-chlorophenyl)-N-methyl-N-(1-methyl-propyl)-3-isoquinoline carboxamide] is the first non-benzodiazepine and selective TSPO ligand developed and labeled with carbon-11. This TSPO antagonist, discovered in 1984 *[55]*, has been the most commonly used TSPO radioligand for in vivo PET imaging or autoradiography *[56]*. However, numerous limitations have been pointed out: low brain uptake, high level of non-specific binding, poor signal-to-noise ratio, that complicates its quantification, extensive binding to plasma proteins, which complicate quantitative analysis of the receptor density and in addition the short half-life of carbon-11 (20.38 min) *[57]*. All these characteristic limit its accuracy, dissemination and wide preclinical and clinical use *[58]*.

Over last two decades, efforts have been undertaken to develop several new TSPO-specific radiotracers, labeled with carbon-11 but also with the longer lived positron-emitter fluorine-18 (109.8 min) in an attempt to avoid some of the limitations observed with [11C]PK11195. Therefore, extensive research has led to the development of new TSPO tracer like [11C]DAA1106, [18F]FEDAA1106, [11C]PBR28 that have been described and reported to display in vivo properties in rodents brains. [11C]DAA1106 and [18F]FEDAA1106 have also been shown to display highly specific in vivo uptake in primate brains. Furthermore, [18F]FEDAA1106 was recently evaluated in human PET studies *[59]*.

In the last decade, a series of TSPO-specific pyrazolopyrimidine ligands were synthesized and in particular one of these tracers, N,N-diethyl-2-(2-(4-methoxyphenyl)-5,7-dimethylpyrazolo [1,5-

a]pyrimidin-3-yl) acetamide (DPA-713), was labeled with 11C. PET studies showed that [11C]DPA-713 selectively and specifically bound the TSPO in normal baboon brains *[60]*. All these encouraging results suggested to synthesize a derivative of DPA-713, the pyrazolo[1,5]pyrimidine DPA-714, labeled with fluorine 18. Fluorine 18 has physical characteristic more favorable than carbon 11, like a longer half-life and lower positron energy. This allows the wide distribution of the radiotracer to sites different from that of synthesis and favors longer scanning time.

## 1.5. [18F]DPA-714 a new suitable radiotracer for PET studies

N,N-diethyl-2-(2-(4-(2-fluoroethoxy)phenyl)-5,7-dimethylpyrazolo[1,5-a]pyrimidin-3-yl)acetamide (DPA-714), a TSPO agonist, was developed and labeled with fluorine 18 (half-life of 109.8 min). In 2008, James ML. et al. studied and evaluated this radiotracer ex-vivo in a neuroinflammatory rat model and in vivo in a healthy baboon using PET. Ex-vivo biodistribution studies in rats showed highest accumulation of [18F]DPA-714 in the heart and adrenal glands, with only minimal accumulation in the bone, liver, and muscle. Pretreatment with DPA-714 (1 mg/kg) resulted in inhibition of radioligand uptake in the heart and partially in the adrenal glands. An elevated uptake was observed in the ipsilateral striatum, as compared to contralateral striatum that was specific since it was inhibited by preinjection of a large dose of unlabeled PK11195, DPA-

714 and DPA-713. In vivo biodistribution and specificity of [18F]DPA-714 were also characterized in a normal male baboon with PET. In a base-line study, the time-activity curves of the whole brain [18F]DPA-714 uptake showed a fast uptake reaching the maximum at 10 minutes after the radiotracer injection followed by a slow wash-out during 60 minutes. Pretreatment with PK11195, five minutes before radioligand injection, resulted in an initial increase of [18F]DPA-714 uptake, followed by a rapid decrease. Displacement with DPA-714 injected 20 minutes after radiotracer, led to a sharp peak followed by a complete washout of [18F]DPA-714. In extracerebral organs, the [18F]DPA-714 uptake was higher in the heart, kidneys, adrenal glands, and salivary glands. The injection of nonlabeled DPA-714, 20 minutes after radioligand administration, displaced [18F]DPA-714 binding in these peripheral regions. These results suggested that [18F]DPA-714 is a high-affinity radioligand specific for TSPO and its ability to bind to TSPO with high specificity, make this ligand an attractive tool for evaluating TSPO neuroinflammatory processes *[59]*. Subsequent in vivo studies with microPET in rat models of NI confirmed the increased binding and the specificity of [18F]DPA-714 in the inflammatory areas *[61-62]*. Moreover these studies compared, in the same model, the sensitivity and the specificity of [18F]DPA-714 to those of other radioligands such as [11C]DPA-713 and [11C]PK11195. The results suggested that in vivo, [18F]DPA-714 performed better than [11C]DPA-713 and [11C]PK11195, with the highest ratio of ipsilateral to contralateral uptake and the highest binding potential in a model of unilateral acute intrastriatal lesion *[61]*. Also Doorduin et al. compared [18F]DPA-714, [11C]DPA-713 and [11C]PK11195 in a rat model of herpes encephalitis and found no

significant difference in sensitivity between the 2 carbon-11-labeled radiotracers, while a better contrast was obtained using [18F]DPA-714 *[62]*. Evaluation of the PBR/TSPO radioligand with [18F]DPA-714 and microPET was also performed in a rat model of focal cerebral ischemia. Significant increase in the specific binding of the radioligand could be measured in the ischemic hemisphere at 7, 11, 15, and 21 days after ischemia reaching the maximum uptake at 11 days. In vitro autoradiography confirmed these in vivo results. In vivo and in vitro [18F]DPA-714 binding was displaced from the lesion by PK11195 and DPA-714. Immunohistochemistry showed that increased TSPO expression was related to activated microglia/macrophage cells in the ischemic area *[63]*.

## 1.6. [18F]DPA-714 in mice

The mouse has become a key model for studying human diseases because of the advantage to be easily maintained in a research services facility with respect to other animal species. Moreover, it could be considered an important surrogate model of genetic and not genetic disorders. Thus, the use of mouse models is of relevance to validate specific TSPO PET radiotracer and to study pathological changes in case of neuroinflammatory disease, in particular when combined with ex-vivo immunohistochemistry. In mice only few studies have been performed with [18F]DPA-714 and microPET and in these studies the in vivo biodistribution and specificity of [18F]DPA-714 binding in normal mouse have not been completely characterized and radiolabeled metabolites were not measured. Ex-vivo biodistribution in mice showed, 60 minutes after the i.v. injection of [18F]DPA-714,

an high uptake in peripheral tissues known to be rich in TSPO with the highest accumulation in the heart, adrenal glands and kidney, whereas very low uptake was found in the brain *[64]*. Identification of radiometabolites of [18F]DPA-714 in the plasma and urines has been reported recently in vivo and in vitro only in rats and in baboons. Ex-vivo studies in rats revealed 15% of radiolabeled metabolite in the brain at 120 minutes after the radiotracer injection *[65]*. Moreover, the specificity and sensitivity of [18F]DPA-714 microPET in detecting NI changes in the SNC of NI models have to be further addressed. Significant increase in [18F]DPA-714 uptake could be measured in the ischemic brain area after transient middle cerebral artery occlusion *[66-67]*. The sensitivity and specificity of [18F]DPA-714 microPET in the study of NI in inflammatory and neurodegenerative models have not yet been reported.

## 1.7. Objective of the thesis

The general aim of the present work was to validate the use of [18F]DPA-714 for the study of TSPO sites in vivo with microPET in mice models of NI.

To this aim, we planned the following studies:

1) Characterization of the in vivo biodistribution, specific binding and ex-vivo radiometabolites of [18F]DPA-714 in normal mouse

2) Characterization of brain TSPO expression in a mouse model of Amyotrophic Lateral Sclerosis using [18F]DPA-714 and microPET and immunohistochemistry.

3) Characterization of brain TSPO expression in a mouse model of Multiple Sclerosis using [18F]DPA-714 and microPET and immunohistochemistry.

All the studies performed were approved by the animal welfare regulation committee (CESA) of the University "Federico II" of Naples and by the Italian Ministry of Health. It complied with the Guide for the Care and Use of Laboratory Animals published by the US National Institutes of Health (NIH Publication No. 85–23, revised 1996).

# 2. Characterization of the in vivo biodistribution, specific binding and ex-vivo radiometabolites of [18F]DPA-714 in normal mouse

The validation of [18F]DPA-714 is mandatory in order to assess whether it is a suitable radioligand for in vivo studies of TSPO sites in the brain and in the extracerebral regions of mice. [18F]DPA-714 has been characterized ex-vivo and in vivo with microPET in experimental models of neuroinflammation in rats. However, very few studies have investigated in detail the biodistribution and the specific binding to TSPO sites. In mice, to our knowledge, only one study *[64]* has previously reported, only in part and ex-vivo, the biodistribution of [18F]DPA-714 in healthy mice, while no in vivo microPET studies are currently available. Moreover, the measurement of radiolabeled metabolites has been done only in rat brain and liver *[65]*. The characterization of radiolabeled metabolites is a crucial step in the development of new radiotracers to better understand the behavior of the unchanged radiolabeled compounds for a more accurate quantification of TSPO.

In this study we have characterized the biodistribution and the kinetics of **[**18F]DPA-714 in the brain and in the peripheral organs of healthy mice and we have evaluated the ability of large amount of unlabeled DPA-714 and PK1195 to inhibit **[**18F]DPA-714 binding using competitive studies. Moreover, we have quantified the presence of the main radiometabolites in different organs.

## 2.1. Materials and methods

### 2.1.1. Mice

Twelve to 18-weeks-old male C57BL/6J mice (body weight: 30.5 ± 4.7) underwent PET/CT exam. Mice were purchased from Charles River Laboratories (MI, Italy) and were housed in Plexiglas cages (36.5×20.7×14.0 cm), subjected to a 12 h light/dark cycle with ad libitum access to water and food (Mucedola® srl, Italy).

### 2.1.2. PET studies: acquisition protocol and image analysis in healthy mice

All the PET studies were performed under anesthesia induced with 2 L/min Oxygen plus Isoflurane 4% and maintained with 2% of Isofluorane delivered by a precision vaporizer (Vetequip incorporated®/Isoflurane vaporizer Funnel-Fill®) with a mice facial anesthesia mask connected to a coaxial non-rebreathing system (Vetequip incorporated®). Dynamic acquisitions (frames sequence: 4×1 min, 3×2 min, 4×5 min, 4×10 min) were performed over 60–70 minutes after intravenous (i.v.) injection of 5.55–7.00 MBq (30–87 pmol), specific radioactivity (SRA) range: 80–300 GBq/μmol, mean ± SD = 120 ± 43 GBq/μmol) of [18F]DPA714 by tail vein, through the use of a catheter.

Biodistribution studies were performed in 5 animals in which, [18F]DPA-714 was injected at trace doses.

Pharmachological blocking studies were performed in 10 animals in order to assess the specific binding to TSPO sites. Intravenous injection of 1 mg/kg of unlabeled DPA-714 (n = 5) or 3 mg/kg of unlabeled PK11195 (n = 5) (PK11195 ABX advanced biochemical

compounds GmbH) was performed 5 minutes before [18F]DPA-714 injection.

For data analysis, time activity curves (TACs) were generated from circular regions of interest (ROI) manually drawn by over PET/CT fused images of brain, lungs, heart, liver, spleen and kidney, using PMOD software (v2.8; PMOD Technologies Ltd., Zurich, Switzerland).

### 2.1.3. Ex-vivo studies: metabolite assay of [18F]DPA-714 in plasma and peripheral tissue of healthy mice

Metabolite assay was carried out in five mice and PET images were also acquired in two of these mice. Sixty minutes after intravenous injection of [18F]DPA-714 mice were anesthetized and sacrificed by cervical dislocation. Brain, heart, lung, liver, kidneys, spleen, blood and urine were quickly removed and stored in ice. All peripheral organs were homogenized and centrifuged at 4° C and the supernatant was collected. The resulting soluble fraction was subjected to reversed phase (RP) high-pressure liquid chromatography (HPLC). The retention time (RT) of [18F]DPA-714 was 16.4 min.

### 2.1.4. Statistical analysis

Analysis of variance (ANOVA) was used to compared mean SUVs obtained at 30 and 60 minutes after the radiotracer injection between organs in the unsaturated group of mice (group 1) and in each organ between group 1, group 2 (saturated with unlabeled DPA-714) and group 3 (saturated with unlabeled PK11195). Least Significant Difference (LSD) post-hoc test was then used to localize differences

between organs and/or groups. The slopes of the SUVs over time were compared in group 1 between organs, and for each organ between the three groups by repeated measures ANOVA.

## 2.2. Results

### 2.2.1. [18F]DPA-714 PET/CT uptake

Ten minutes after [18F]DPA-714 i.v. injection in C57BL/6J mice the highest concentration expressed as SUV, was observed in the lungs, followed by heart, kidneys, spleen and liver, while the brain presented the lowest SUV values. Radiotracer clearance was faster in the lung than in the brain and heart, whereas spleen concentration remained almost constant for the entire duration of the exam. In contrast, tracer concentration increased in kidneys and in liver. At 30 min after [18F]DPA-714 injection, activity was reduced to 64% of the 10 min value in the lung, 71% in the brain and 90% in the heart while in the kidneys and in liver increased to 34% of the 10 min values (Fig. 7 A). Repeated measures ANOVA showed that the slopes of the SUVs over time significantly decreased in lung, brain and heart ($p<0.0001$) whereas they significantly increased in spleen ($p<0.05$), kidneys ($p<0.0001$) and liver ($p<0.005$). The organ/brain ratios were significantly lower ($p<0.001$ at ANOVA followed by LSD post-hoc tests) in liver, compared to those of lung, heart and kidneys at 30 min, and significantly higher in kidneys compared to all other organs at 60 min post-injection.

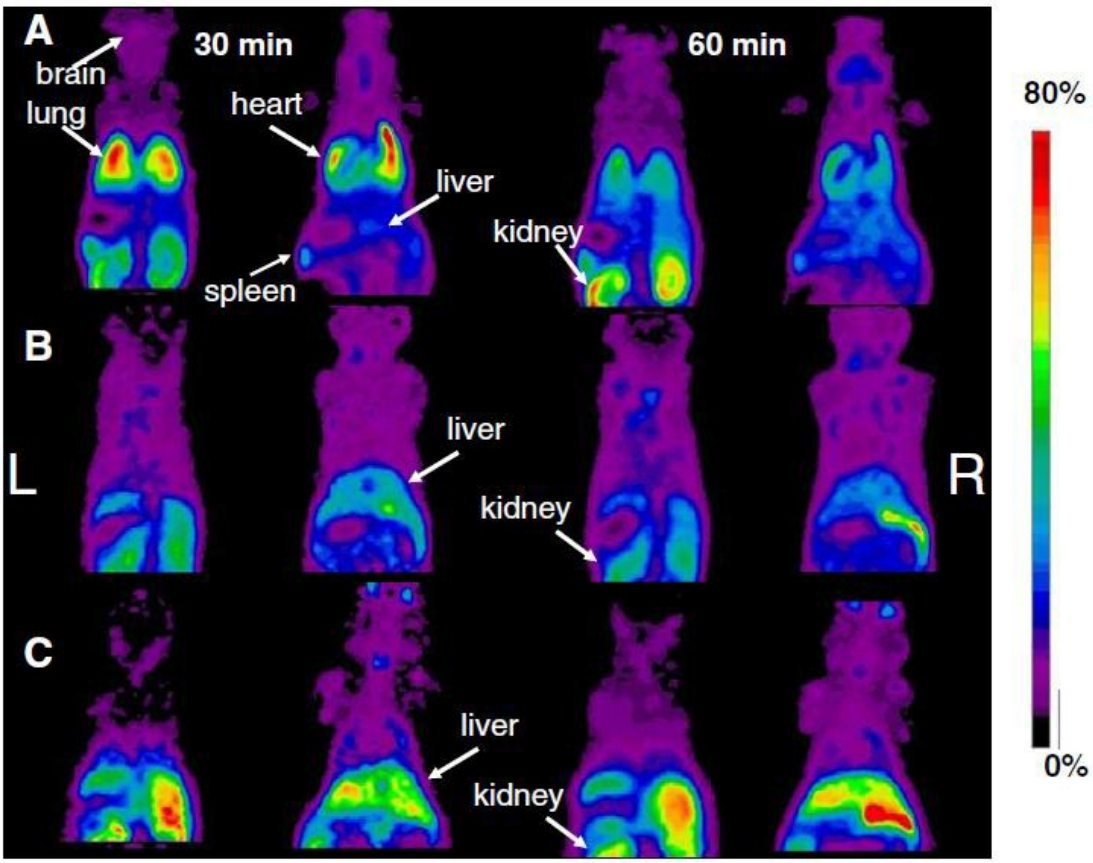


**Fig 6.** Representative coronal PET images at the level of lungs and kidneys (first and third columns) and heart (second and fourth columns), at 30 and 60 minutes (on the left and on the right respectively) post-injection of [18F]DPA-714. Scans were performed at trace dose (A), after pre-injection of 1mg/kg of DPA-714 (B) and of 3mg/kg of PK11195 (C). R and L indicate right and left side of animals *(Vicidomini et al. 2015) [68]*.

### 2.2.2. Blocking studies with DPA714 and PK11195

Pre-injection of large doses of unlabeled DPA-714 (Fig. 7B) and PK11195 (Fig. 7C), dramatically reduced heart and lung radiactivities at 30 and 60 min post-injection. In contrast, kidneys uptake was reduced at 60 minutes post-injection with DPA-714, but not with PK11195, while liver activity was increased, although not significantly. Statistical analysis confirmed these visual findings. The

wash-out of the radiotracer in lung and heart was significantly slower in the blocking studies ($p<0.001$) compared with unblocked studies (group 1), while the increase of radioactivity over time in spleen was significantly ($p<0.05$) reduced in the blocking studies.

A) [$^{18}$F]DPA-714

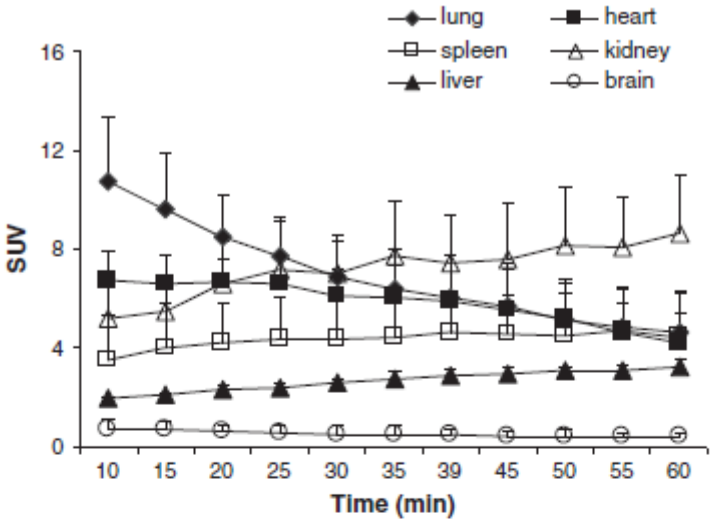


B) [$^{18}$F]DPA-714 + DPA-714 (1mg/kg)

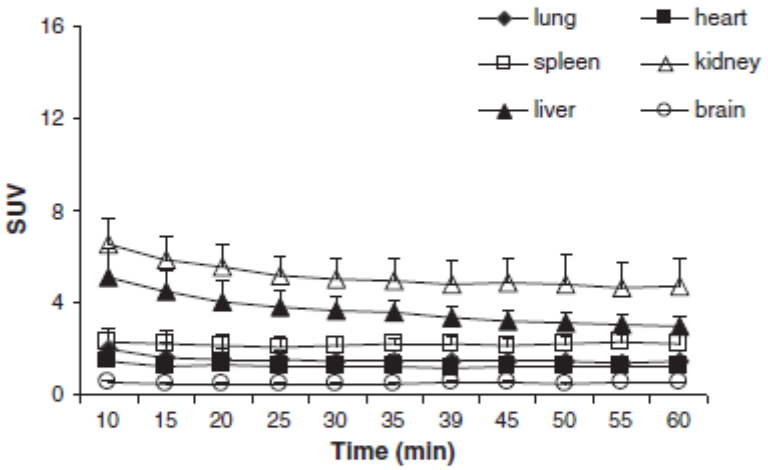


C) [$^{18}$F]DPA-714 + PK-11195 (3mg/kg)

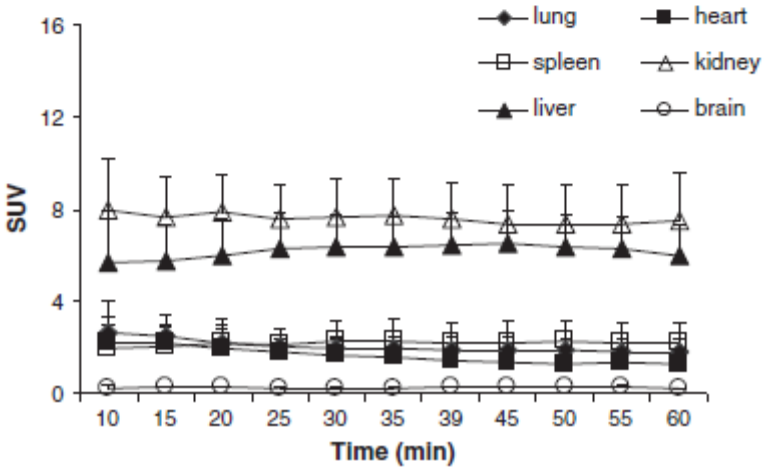

**Fig 7.** Time activity curves (mean ± SD) of SUV values after [18F]DPA-714 injection at trace dose (A), and after pre-saturation of TSPO binding sites with DPA-714 (B) or PK11195 (C), injected 5 minutes before the radioligand *(Vicidomini et al. 2015) [68]*.

Resulting mean SUV values at 30 and 60 min showed significant difference at ANOVA between unsaturated and blocking studies in all regions (p range: 0.05–0.0001). Post-hoc analysis revealed that at 30 min after the radiotracer injection in comparison to group 1, SUV values were significantly reduced in group 2 and 3 in lung (−79%, $p<0.0001$; −72%, $p<0.0001$ respectively), heart (−80%, $p<0.0001$, 72%, $p<0.0001$ respectively) and spleen (−52%, $p<0.05$, −47%, $p<0.05$). In contrast, in kidneys SUV values were significantly reduced in group 2 (-29%, $p<0.05$) and non-significantly increased in group 3 (+9%, $p=0.5$). This resulted in a significant difference between group 2 and 3 ($p<0.01$). In liver, there was an increase of SUV value in group 2 and 3 as compared to group 1, significant only in group 3 (+40 %, $p=0.09$,+146%, $p<0.001$. respectively). In group 3 the SUV values were also significantly higher than in group 2 ($p<0.001$). SUV values of brain were also reduced in group 2 and 3 in comparison to group 1 but only the reduction of 3 group is significant (−18%, $p=0.232$; −53%, $p<0.01$ respectively).

### 2.2.3. Metabolite assay

No measurable radiometabolites were identified at 60 min in brain, lung, spleen and heart. In kidneys, a radiometabolite was observed at RT 14.7 minutes. In liver, two radiometabolites were identified at RT 13.4 and 15.1 minutes, representing averaged values of 3.8% and 11.5% of the total radioactivity, respectively.

## 2.3. Summary and discussion

In this study we have characterized the in vivo biodistribution and specific binding of [18F]DPA-714 in the brain and in peripheral tissues of normal mice using microPET/CT. We showed that [18F]DPA-714 uptake was high in the lung, heart and kidney, intermediate in the spleen and very low in the brain. The regional time-activity curves revealed that the wash-out of [18F]DPA-714 is different among regions: faster in the lung, heart and brain and slower in the spleen and kidney. More importantly, blocking studies revealed that [18F]DPA-714 could significantly and highly inhibited in all these regions. Overall these results demonstrated that the binding of [18F]DPA-714 is specific for TSPO sites. The regional biodistribution of [18F]DPA-714 observed in healthy mice is consistent with previous in vitro and ex-vivo findings on TSPO localization in the brain and in the peripheral tissues of rodents, using other radiotracers *[49-69-70]*. The uptake of [18F]DPA-714 is also consistent with the distribution of [18F]DPA-714 in ex-vivo studies of mice *[64]* and in vivo studies of rats *[49]*. The kinetic studies of [18F]DPA-714 showed that radiotracer uptake in heart at late times was lower than that in lungs, a finding in apparent discrepancy with previous data in primates *[59-65]* and in healthy volunteers *[64]*. This discrepancy might be in part explained by partial volume effects due to the low spatial resolution of micro-PET camera used, with respect to small size of cardiac wall, a region rich in TSPO receptor resulting in underestimation of heart SUV.

Blocking studies confirmed the specificity of [18F]DPA-714 binding for TSPO in mice, in particular pre-injection of unlabeled DPA-714 or

PK11195 reduced radiotracer uptake by 80% and 72% respectively in lung and heart at 30 minutes after injection, by 2% and 47% in spleen and by 17% and 46% in brain. The behavior of DPA714 and PK11195 was different in blocking studies in the kidney where pre-injection of DPA-714 but not of PK11195 significantly reduced [18F]DPA-714 uptake of by 29% and 46% at 30 and 60 minutes, respectively. Another important result was that at 30 and 60 minutes unlabeled PK11195, but not DPA-714, reduced [18F]DPA-714 uptake in the brain *[68]*. These discrepancies could be in part attributed to binding at different sites on the TSPO macromolecule, different metabolism rates and/or different blood kinetics.

In this study we also showed that radioactivity in brain, lung, heart and spleen was essentially due to the intact form of [18F]DPA-714 and not to radiolabeled metabolites. The lack of measurable amount of radiometabolites in brain at 60 min is in part attributable to the presence of only 15% of radiometabolites in the brain of rats at 120 min after [18F]DPA-714 injection *[65]*. However, it should be considered that minimal discrepancies might be due to different methods used. Our method was a little less sensitive than that used in the previous rat study *[65]*. In the kidneys there was a small amount of one radiometabolite at RT 14.7 minutes, while in the liver we found two radiometabolites at RT 13.4 and RT 15.1 minutes (3.8% and 11.5% of the total radioactivity, respectively). To date, radiometabolites of [18F]DPA-714 have been tested in blood samples of rats and baboons, in rat brain homogenates *[61-65]* and in rat and human liver microsomes *[65]*.Thus our results provide additional new informations useful for future use and quantification of [18F]DPA-714 in healthy mice and in animal mice models.

The results of this study have been the object of a publication:

Vicidomini C, Panico M, Greco A, Gargiulo S, Coda AR, Zannetti A, *et al*. In vivo imaging and characterization of [18F]DPA-714, a potential new TSPO ligand, in mouse brain and peripheral tissues using small-animal PET. Nucl Med Biol 2015; 42: 309-16 *[68]*.

# 3. Characterization of brain TSPO expression in a mouse model of Amyotrophic Lateral Sclerosis using [18F]DPA-714 and microPET and immunohistochemistry.

PET imaging and TSPO radiotracers such as [11C]PK11195 and [18F]DPA-714 have been first used in patients with sporadic ALS and provided evidence of increased binding in different cerebral regions including motor cortex, prefrontal cortex and thalamus *[2]*. In a pioneering study in ALS patients, using PET and [11C]PK11195, revealed a significant increased binding in the motor cortex, pons, dorsolateral prefrontal cortex and thalamus *[71]*. More recently, using a second-generation TSPO radioligand such as [18F]DPA-714 and [11C]PBR28, increased binding was confirmed in similar brain regions, compared to healthy controls *[72-73]*. Post-mortem studies using [3H]PK11195 and [3H]DAA1106 in tissues from patients with ALS, showed that in the motor cortex specific binding of both ligands correlated with the presence of activated microglia identified by immunohistochemistry with CD68 antibody *[74]*. To our knowledge, no in vivo studies have demonstrated that increased TSPO expression in the brain and in the spinal cord of ALS might be related to microglial activation. The use of animal models is of relevance for validation of PET TSPO radiotracers, in particular when combined with immunohistochemistry, because allows characterization of histopathological and cellular changes underlying in vivo PET images. Moreover, it could be a useful tool for monitoring NI changes from the presymptomatic stage and the evaluation of the effects of therapy.

In this study, we have characterized both in vivo with PET/CT and [18F]DPA-714, and ex-vivo with immunohistological analysis the TSPO expression and microglial activation in the SNC of transgenic SOD1 G93A mice, the most used and well characterized model of ALS.

## 3.1. Materials and methods

### 3.1.1. SOD1 G93A transgenic mouse model

Experiments were carried out in adult male transgenic hemizygous B6SJL-Tg[SOD1*G93A]1Gur/J mice (SOD1 G93A; stock number 002726), expressing a high copy number (about 29) of the mutant human SOD1 allele with a Gly93Ala substitution, that are characterized by survival times of 128.9±9.1 days. Transgenic hemizygous B6SJL-Tg(SOD1)2Gur/J (WT SOD1; stock number 002297), carrying the normal allele of the human SOD1 gene, served as controls for the SOD1 G93A strain, as it has been reported that WT SOD1 mice express the same level of SOD1 protein as SOD1 G93A mice and do not develop MN degeneration *[24])*. Mice were purchased from Jackson Laboratories (Bar Harbor, ME) via Charles River (Calco, LC, Italy) and were housed in group cages under a 12h/12h light/dark cycle and were allowed free access to food and water.

Disease progression and clinical score: to determine disease onset and progression, mice were monitored three times a week starting at 50 days of age using the clinical score system (CS) described by Solomon et al *[75]*. A numerical scale from 0 to 5 was used to identify the severity of disease: 0 no evidence of disease, 1 shaking or splaying

of the hind limbs when suspended by the tail, 1.5 weakness in one hind limb, 2 change in gait (toes curl under at least twice during walking, or any part of foot is dragging along cage bottom/table), 2.5 extreme weakness in one hind limb, 3 extreme weakness in both hind limbs, 3.5 functional paralysis in one hind limb, 4 functional paralysis in both hind limbs but can right themselves in less than 20 seconds after being placed on their side, 5 cannot right themselves to sternum within 20 seconds after being placed on their side (endpoint) *[75]*. SOD1 G93A mice with advanced symptoms of ALS had a source of hydration and energy placed on the cage floor, and electrolyte balanced solutions were provided parenterally. Body weight and body condition score were evaluated three times a week, as described elsewhere *[75]*. Mice were euthanized after reaching a score of 4 according to the guidelines for preclinical testing and colony management *[76]*.

### 3.1.2. PET studies: acquisition protocol and image analysis for G93A SOD1 mouse model

Nine symptomatic SOD1 G93A mice aged from 117 ± 12.75 days (mean age ± SD) with CS ranging from 1 to 4 and five congenic controls WT SOD1 aged from 108 ± 28.5 days were anesthetized as reported in paragraph *2.1.2* and underwent PET/CT. Images were acquired in dynamic mode (frame sequence: 6×5 min) over 30 min starting 20 min after injection via a tail vein of 5.55–7.00 MBq (specific radioactivity 200–800 GBq/μmol) of [18F]DPA-714. Count rates were converted to SUV and PET frames acquired between 20 and 50 min were summed and used for data analysis. Regions of

interest (ROIs) were manually defined on summed axial PET images based on PET/CT fusion images using the mouse brain atlas of Paxinos and Franklin for guidance *[77]*. ROIs were placed on cerebellum, brainstem, upper part of the cervical spinal cord, motor frontal cortex and frontal association cortex, over at least three consecutive slices using OsiriX 5.8.5 imaging software (Pixmeo, Bermex, Switzerland). For each brain region, [18F]DPA-714 SUVs were calculated by pooling the ROIs defined over consecutive slices. SUV ratios were calculated by normalizing the cervical spinal cord (rCSC), cerebellar (rCRB), brainstem (rBS), and motor cortex (rMCX) activities to that of the frontal association cortex. This normalization was performed to reduce between-animal variability in radiotracer uptake. The frontal association cortex was used for normalization because this region is unaffected in SOD1 G93A mice.

### 3.1.3. Ex-vivo studies: SOD1 G93A mice tissue processing for immunohistochemical studies and confocal acquisition

Prefrontal cortex, motor cortex, cerebellum, brainstem motor nuclei and cervical, thoracic and lumbar tracts of spinal cord were analyzed.
Two control WT SOD1 and six symptomatic SOD1 G93A mice, one CS of 2, one CS of 2.5 and four CS of 4 (median CS 4), were studied. All animals underwent PET from 1 to 9 days before euthanasia (mean ± SD 5 ± 3 days) except one SOD1 G93A mouse with a CS of 2. In one of the symptomatic SOD1 G93A mice with a CS of 4 only the motor cortex and spinal cord were available for immunofluorescence. For the exact anatomical identification we used the mouse brain atlas

of Paxinos and Franklin *[77]*. Images were observed using a confocal microscope Zeiss LSM 700.

### 3.1.4. Statistical analysis

Descriptive statistics for body weight, BCS and CS was performed in both SOD1 G93A and WT SOD1 mice. The clinical and [18F]DPA-714 SUV data were analyzed using the software package SPSS version 11 (SPSS, Chicago, IL). The nonparametric Mann-Whitney test was used to compare [18F]DPA-714 SUVs of the frontal association cortex, and rCSC, rCRB, rBS and rMCX between SOD1 G93A and WT SOD1 mice. The nonparametric Spearman's rank correlation coefficient was used to determine the correlation between age and CS and regional SUV ratios in SOD1 G93A mice. The level of significance was set at $p \leq 0.05$.

## 3.2. Results

### 3.2.1. Clinical score and body weight

SOD1 G93A mice became symptomatic from 95 days of age (mean ± SD: 102.8 ± 7.04 days, range 95–110 days) and progressively worsened (CS score from 1 to 4, and BCS score from 3 to 2). WT SOD1 controls remained healthy (CS 0, BCS 3). The average body weight in SOD1 G93A mice was significantly lower than that of WT SOD1 mice from the age of 14 weeks (mean ± SD: 26.55 ± 2.49 g vs. 31.29 ± 1.84 g, respectively; $p = 0.027$), with the difference in body weight increasing with disease progression (Fig 8).

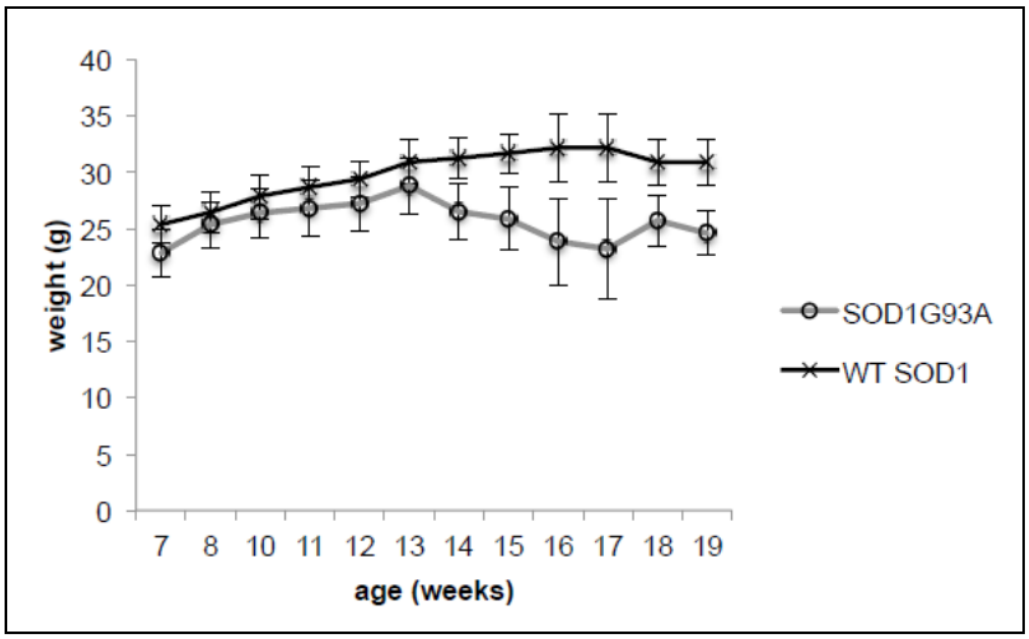


**Fig. 8** Body weight (mean±SD) registered from 7 to 19 weeks of age in SOD1 G93A and WT SOD1 mice (*Gargiulo et al. 2016 Electronic supplementary material*) *[87]*.

### 3.2.2. [18F]DPA-714 PET/CT uptake

PET images showed a clear increase of [18F]DPA-714 uptake in brainstem and in cervical tract of spinal cord of symptomatic SOD1 G93A mice as compared to WT SOD1 mice while the uptake in the anterior cerebral regions appeared lower (Fig. 9).

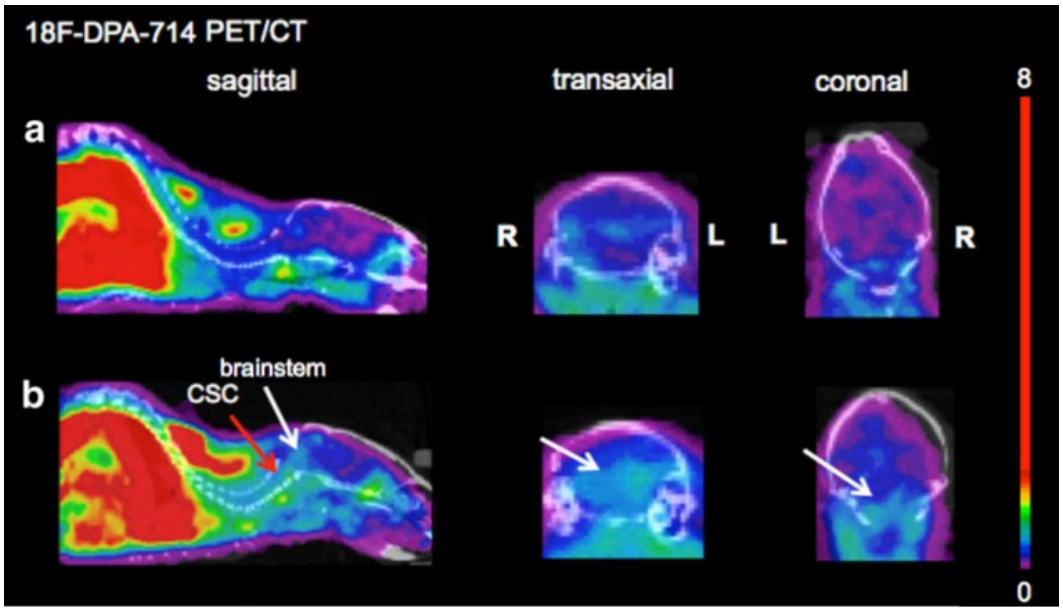


**Fig. 9** Representative PET/CT fusion images at the level of brainstem in a WT SOD1 control mouse (a) and in a symptomatic SOD1 G93A mouse, obtained from summation of scans between 20-50 min after [18F]DPA-714 injection. SUV values were normalized to those of the frontal association cortex and scaled at a maximum value of 8. A higher radiotracer uptake is evident in the brainstem of symptomatic mouse (white arrows) as compared to control mouse. Red arrow shows an increased uptake also in cervical spinal cord in sagittal view of symptomatic SOD1 G93A mouse.

Since differences between average SUV of frontal association cortex in SOD1 G93A and WT SOD mice, were not significantly (0.207 ± 0.090 and 0.225 ± 0.105, respectively; $p = 0.787$), we used this region as reference to generate regional SUV ratios. In symptomatic mice, the regional SUV ratios were significantly increased compared with WT SOD1 controls only in rBS (2.340 ± 0.784 and 1.576 ± 0.287 respectively, $p = 0.014$). The rCSC mean values were increased by 59 % in symptomatic SOD1 G93A mice as compared to WT SOD1 controls, but the averaged values (3.243 ± 1.408 and 2.084 ± 0.551 respectively) were not significant ($p = 0.053$). Similarly, no significant differences between symptomatic SOD1 G93A mice and WT SOD1

controls were found in rCRB (2.063 ± 0.612 and 1.691 ± 0.364 respectively, p=0.162) and rMCX values (1.090 ± 0.242 and 0.928 ± 0.101 respectively, p=0.162). In symptomatic SOD1 G93A mice, CS showed a statistically significant correlation with age ($R = 0.786$, $p \leq 0.05$), whereas there was no significant correlation between CS and [18F]DPA-714 SUV ratios (Fig. 10).

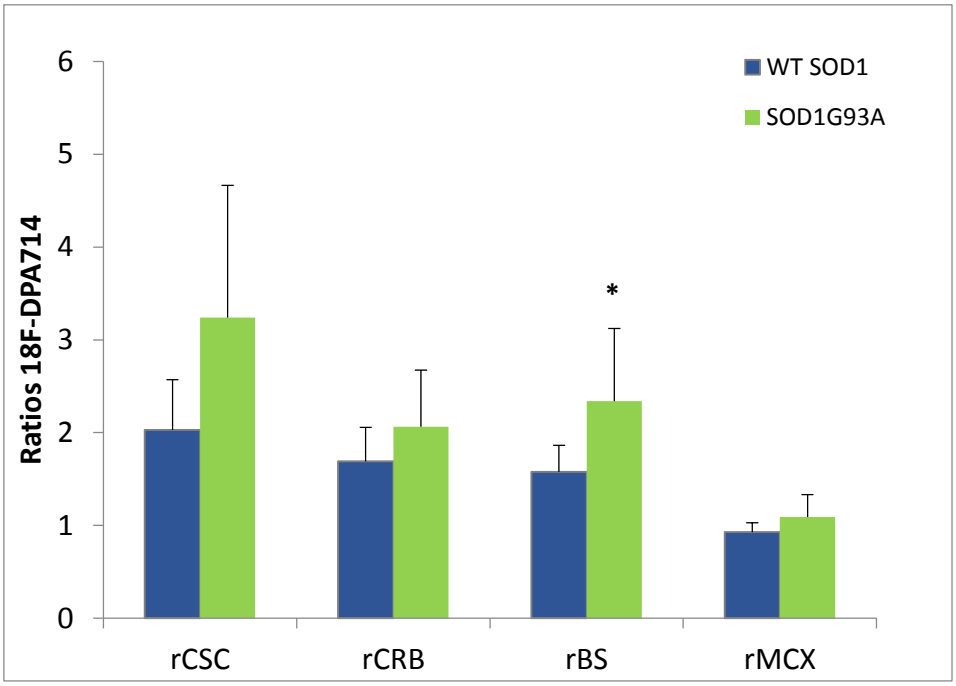


**Fig 10** [18F]DPA-714 SUV values reported in histogram for cervical spinal cord (rCSC), cerebellum (rCRB), brainstem (rBS) and motor cortex (rMCX) in WT control mice compared to symptomatic G93A SOD 1 mice (*p<0.02).

### 3.2.3. Immunohistochemistry

Increased expression of TSPO in Iba1 positive cells was found in the brainstem of symptomatic SOD1 G93A mice, while in WT SOD1 controls, Iba1 and TSPO immunolabeling were weak. In particular, in SOD1G93A mice with CS of 4 a strong increase of Iba1 positive cells

was observed in the trigeminal, facial, ambiguus, hypoglossal nuclei. Iba1 positive cells showed a clear morphological change characterized by enlargement of body cell and shortening of cellular processes. Moreover, activated microglial cells revealed a perfect colocalization with TSPO immunoreactivity (Fig. 11). Iba1 and TSPO expression was also higher in SOD1 G93A mice with a CS of 2 – 2.5 than in WT SOD1 controls, although the difference was not as great as in SOD1 G93A mice with a CS of 4.

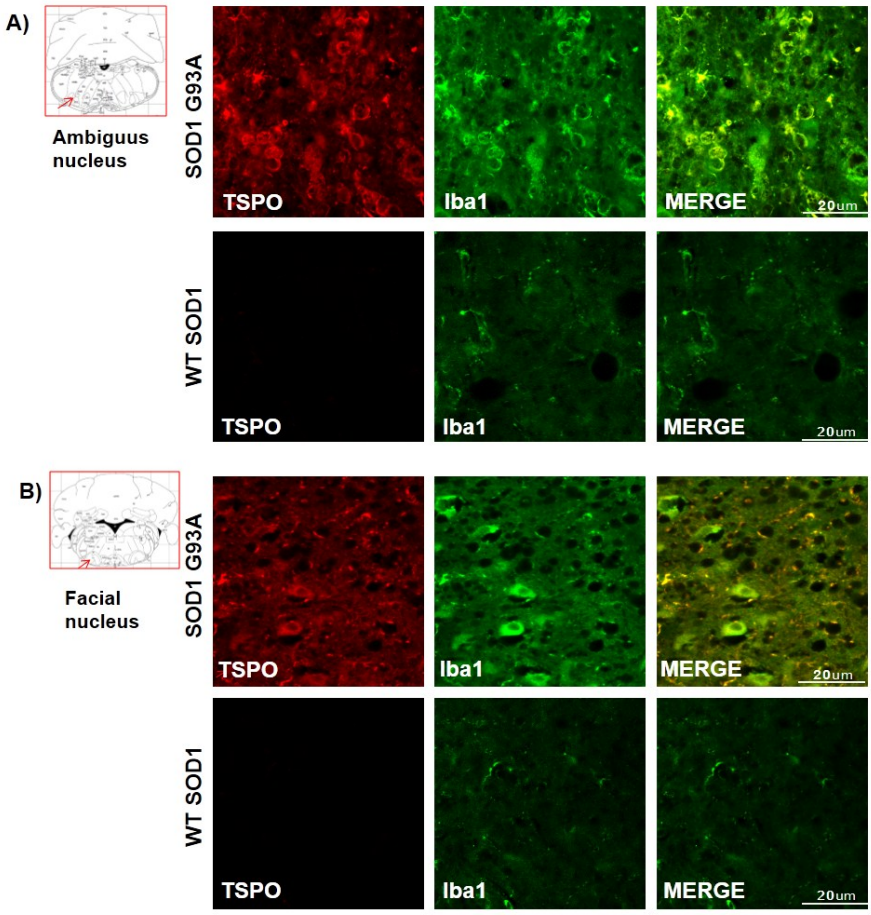


**Fig 11** Confocal laser scanning microscopy images of TSPO and Iba1 immunofluorescence in ambiguus nucleus (A) and facial nucleus (B) of a symptomatic SOD1 G93A at CS 4 and a WT control mouse. TSPO immunolabeling (in red), Iba1 immunolabeling (in green) and merged images (in orange).

Elevated expression was also found in motor cortex (Fig. 12 A) and in cerebellum (Fig. 12 B). However, Iba1 and TSPO expression in the frontal association cortex was not present in SOD1 G93A mice and in WT SOD1 controls (data not shown).

Increased Iba1 and TSPO expression could be also clearly observed in the cervical (Fig. 12 C), thoracic and lumbar tracts of spinal cord in SOD1 G93A mice compared to controls, more marked in animals with CS of 4.

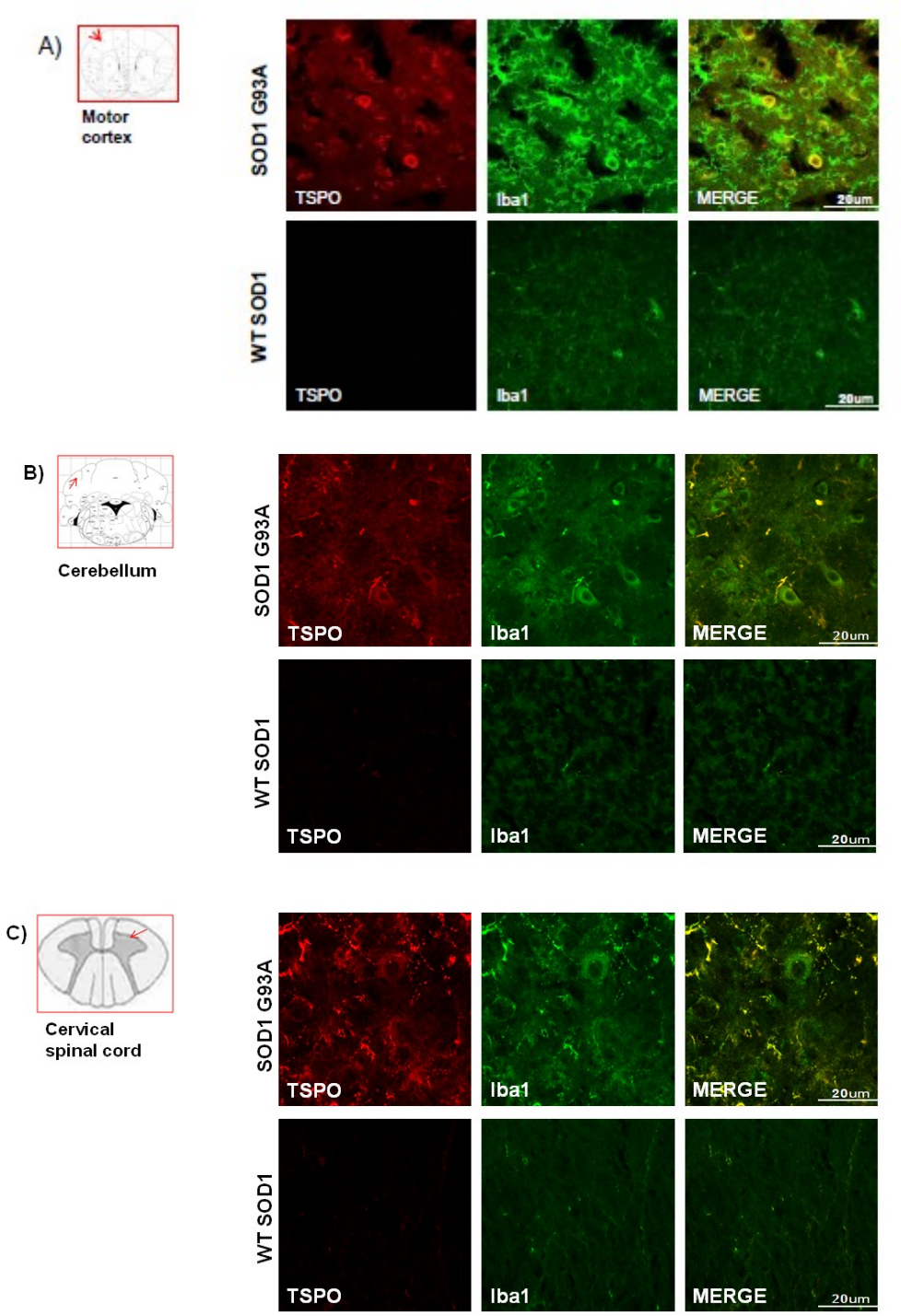


**Fig. 12** Confocal laser scanning microscopy images of TSPO and Iba1 immunofluorescence in motor cortex (A), cerebellum (B) and cervical spinal cord (C) of a symptomatic SOD1 G93A at CS 4 and a WT control mouse. TSPO immunolabeling (in red), Iba1 immunolabeling (in green) and merged images (in orange).

## 3.3. Summary and discussion

The results of this study are the first to be reported in SOD1 G93A mice, a model of ALS, using microPET, a radioligand for TSPO sites and immunohistochemistry. They suggest that a significant increase in [18F]DPA-714 uptake can be measured in vivo with high-resolution PET/CT in the brainstem of symptomatic SOD1 G93A mice. Moreover, immunostaining showed that increased TSPO expression in the brainstem nuclei was colocalized with Iba1 immunoreactivity, underlying the important contribution of microglial activation to the increased brainstem [18F]DPA-714 uptake. In contrast, transgenic mice over-expressing the nonmutated wild-type human SOD1 did not show increased [18F]DPA-714 uptake in vivo as well as increased TSPO and Iba1 expression ex-vivo. The low spatial resolution of PET scanner did not allow identifying individual brainstem nuclei, instead the combined results with immunofluorescence studies demonstrated that increased TSPO and Iba1 expression in specific motor nuclei, such as the trigeminal, facial, ambiguus and hypoglossal, might underlie increased [18F]DPA-714 brainstem binding measured in vivo in symptomatic SOD1 G93A mice.

Our findings are in line with previous post-mortem studies showing that these brainstem nuclei are site of strong inflammatory reaction in SOD1-ALS transgenic mice. Interestingly, in the same brainstem nuclei post-mortem studies *[78-79]*, and in more recent in vivo MRI studies *[80],* degenerative changes were markedly showed, suggesting a link between NI and neurodegeneration of motor nuclei in this ALS model. Inflammatory changes seem to appear earlier than neurodegenerative changes, suggesting that NI even in neurodegenerative disorders might be an interesting therapeutic target.

Previous studies indicated that SOD1-ALS transgenic mice also show more widespread inflammatory changes involving other brain regions than the spinal cord and brainstem including the cerebellum *[80-81]* and the motor cortex *[82-83]*. Nevertheless, in this work [18F]DPA-714 binding in the cerebellum and motor cortex showed no significant increase. Only in two symptomatic SOD1 G93A mice, with severe clinical score, ex-vivo immunohistochemistry showed increased Iba1 and TSPO immunoreactivity in motor cortex in one and in the cerebellum in the other one. Further studies are recommended. We failed to measure with PET significant in vivo changes in [18F]DPA-714 uptake in the spinal cord. This is in contrast with our results of immunostaining performed in the same animals and showing increased TSPO expression in the entire spinal cord, accompanied by a good colocalization with Iba1 immunoreactivity in agreement with previous postmortem findings of increased microglial expression in spinal cord of transgenic SOD1 G93A mice *[84-85],* and more recent in vivo PET data showing increased [11C]PBR28 binding in the spinal cord of symptomatic SOD1 G93A mice *[86]*.

This suggests that PET with [18F]DPA-714 is not sensitive enough to detect microglial activation and increased TSPO expression in mice, at least at the cervical level using our microPET camera.

The results of this study have been the object of a publication: Gargiulo S, Anzilotti S, Coda AR, Gramanzini M, Greco A, Panico M, et al. Imaging of brain TSPO expression in a mouse model of amyotrophic lateral sclerosis with 18F-DPA-714 and micro-PET/CT. Eur J Nucl Med Mol Imaging 2016, 43: 1348-1359 *[87]*.

# 4. Characterization of brain TSPO expression in a mouse model of Multiple Sclerosis using [18F]DPA-714 and microPET and immunohistochemistry.

In MS animal models, PET studies have been undertaken to monitor NI changes using glucose metabolism and more recently specific TSPO PET radioligands *[88]*. Increased [18F]FDG PET uptake was reported in spinal cord of C57BL/6 mice from day 8 to 21 after immunization *[89]* and of dark agouti rats between 10-14 days from immunization *[90]* with MOG peptide, an EAE chronic-progressive model. The increased [18F]FDG uptake was associated with the presence of inflammatory infiltrates as determined by histology *[89-90]* and correlated especially with CD68-positive cells in rats *[90]*. Moreover, immunosuppressive therapy with dexamethasone, performed in mice, reduced glucose metabolism in the spinal cord *[89]*. Although the changes in glucose metabolism detected with [18F]FDG and anatomical location of the PET signal are suggestive of the presence of inflammatory infiltrates, this radiotracer is not a specific marker of NI. Other important limits are the high background activity in the CNS due to the high physiologic glucose consumption of the brain and the lack of specificity for glial cells.

Recently, PET studies in different EAE rats and mice models have focused on the evaluation of more specific molecular biomarkers of cells involved in NI, in particular microglia and astrocytes, such as TSPO. Among these, [18F]DPA-714 has been also applied to explore the expression of TSPO in a rat model of acute monophasic EAE-

MBP. The distribution of radioactivity showed an increased uptake in thoracic and lumbar spinal cord, fivefold higher than control animals. The specificity of [18F]DPA-714 binding was confirmed in competition studies, using unlabeled PK11195 or DPA714. Moreover, immunohistochemical staining showed that TSPO expression colocalized with activated microglia and macrophages, but not with astrocytes. In this study the binding of [18F]DPA-714 was not investigated in the brain because inflammatory changes in this model are prevalent in the spinal cord *[91]*.

The sensitivity of [18F]DPA-714 and microPET has not been assessed in mice MS models and in particular in EAE model associate to both spinal cord and brain NI changes.

In this study, we have characterized both in vivo with PET/CT and [18F]DPA-714, and ex-vivo with immunohistological analysis the TSPO expression and microglial activation in the SNC of an EAE model induced in SJL/J by mice immunized with PLP. This model mimics the relapsing remitting clinical form of human MS and involves both the spinal cord and brain regions *[92]*.

## 4.1. Materials and methods

### 4.1.1. EAE mouse model and induction of disease

Female SJL/J mice at 6 weeks of age were purchased from Charles River (Calco, LC, Italy) and were housed in group cages under standard conditions with free access to food and water. Mice were

allowed to acclimatize for one week before the start of any experiment.

On day 0, EAE symptomatic animals were subcutaneously immunized at each of two sites at the base of the tail with an emulsion of equal volumes of the proteolipid protein $PLP_{139-151}$ (Inbios) in complete Freund's adjuvant (CFA, Becton Dickinson Italia) supplemented with 4mg/ml inactivated Mycobacterium tuberculosis H37RA (Becton Dickinson Italia). The initial immunization was followed by intraperitoneal administration of 2ng/ml Bordetella pertussis toxin (BPX, Sigma Aldrich) in PBS (phosphate buffered saline) on the same day (day 0) and the following day (day 1). During all procedures of immunization, mice were gently handled, to avoid stress and anesthesia was not used. In some mice, obvious bumps developed at the injection sites 2 to 4 days after immunization. Rarely alopecia developed at the site of injection. Control animals received same procedures of immunization, but $PLP_{139-151}$ were replaced with PBS *[93]*.

Neurological assessment and clinical score: animals were monitored at least daily, every day including weekends. Clinical signs began with motor deficits characterized by an ascending paralysis starting from the tail. Animals with initial symptoms were isolated in separate cages with easier access to food and water, and all dehydrated animals received an intraperitoneal injection of saline solution at least once a day. Clinical signs were graded on a five-point scale: 0 no obvious changes in motor function, 0.5 tip of tail is limp, 1 limp tail, 1.5 hind leg inhibition, 2 weakness of hind legs, 2.5 dragging of hind legs, 3 paralysis of hind legs, 3.5 hind legs are completely paralyzed and together on one side of body, 4 complete hind leg and partial front leg

paralysis, 4.5 no movements around the cage, euthanasia is recommended, 5 death due to paralysis *[94]*.

### 4.1.2. PET studies: acquisition protocol and image analysis for EAE mouse model

Seventeen EAE symptomatic mice from 11 to 25 days post immunization, with CS ranging from 0 to 4 and seven control mice were anesthetized with isoflurane and injected via tail vein, with 5 – 10 MBq (specific radioactivity 200–800 GBq/μmol) of [18F]DPA714. PET acquisition started 20 minutes after radiotracer injection and lasted 30 minutes. Images were acquired in dynamic mode (frame sequence: 6×5 min) ROIs were manually defined on summed images based on PET/CT fusion images using the mouse brain atlas of Paxinos and Franklin for guidance *[77]*. Circular ROIs were placed on the olfactory bulbs (OB), prefrontal cortex (PFC), cerebellum (CBR), brainstem (BS) and the upper part of cervical spinal cord (CSC) using PMOD imaging software. Also for this model, as for G93A SOD1 transgenic mice, thoracic and lumbar spinal cord were excluded from analysis because their small size can be influenced by partial volume effects. SUV ratio values were obtained using frontal cortex value to normalize values of all other regions (rOB, rCBR, rBS, rCSC). Frontal cortex is unaffected region in EAE $PLP_{139-151}$ and it did not show significant differences between symptomatic and control mice. Thus, it was used as reference for normalization.

### 4.1.3. Ex-vivo studies: EAE mice tissue processing for immunohistochemical studies and confocal acquisition

After in vivo studies, EAE symptomatic and control mice were anaesthetized with isoflurane 4%, transcardially perfused and underwent to the same procedures for ex-vivo studied used for SOD1 G93A mouse model.

Five control EAE mice and seven symptomatic EAE mice, one CS of 0.5, one 1.5, one CS of 2.5, three CS of 3.5 and one CS of 4 (median CS 3.5), were analyzed. All animals underwent PET studies before euthanasia for ex-vivo studies. Frontal motor cortex, corpus callosum, striatum, cerebellum, brainstem and cervical, thoracic and lumbar tracts of spinal cord were analyzed. The mouse brain atlas of Paxinos and Franklin was used for a correct identification of all regions *[77]*.

### 4.1.4. Statistical analysis

Non parametric Mann-Whitney test was used to compare [18F]DPA-714 SUV values of region/prefrontal cortex ratios between EAE symptomatic and control mice. In addition, Pearson's correlation coefficient was used to determine the correlation between clinical score and regional SUV ratios in all EAE mice (clinical score range: 0-4). The level of significance was set at $p \leq 0.05$.

## 4.2. Results

### 4.2.1. Clinical score and body weight

EAE mice became symptomatic between the tenth and the eleventh days after $PLP_{139-151}$ immunization, followed by a peak between the twelfth and fifteenth days and a subsequent recovery that was almost complete from 16 until 25 days, the last day of our study (Fig. 13).

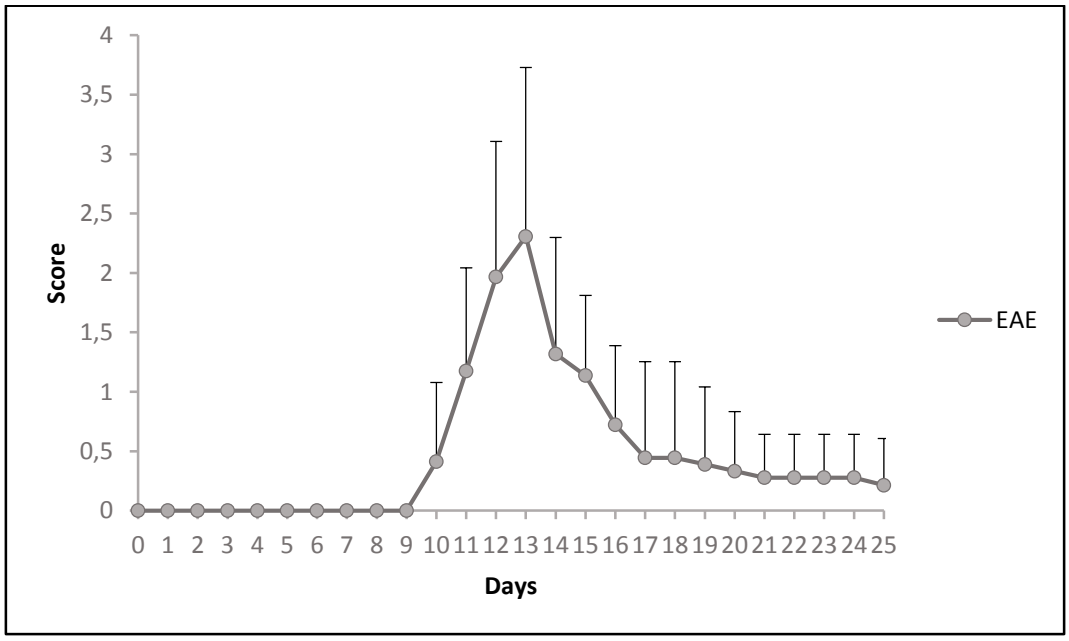


**Fig 13** Clinical score (mean±SD) registered from 0 to 25 day after immunization in EAE mice.

Weight of EAE animals started to decrease just before the appearance of the first clinical symptoms and then recovered when the mice became asymptomatic (Fig. 14).

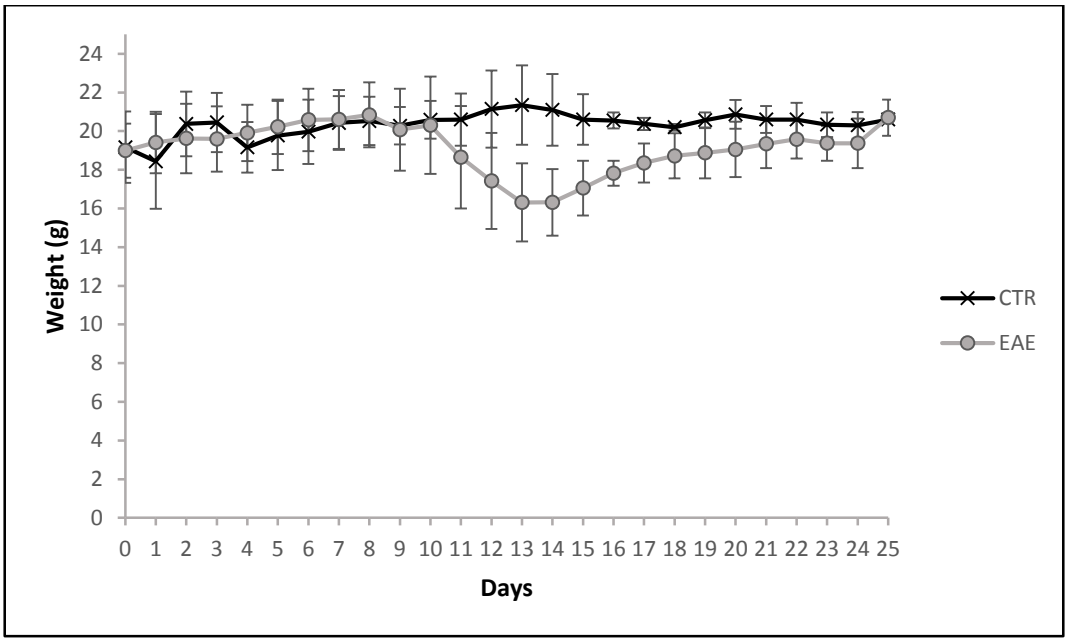


**Fig. 14** Body weight (mean±SD) registered from 0 to 25 day after immunization in EAE and control mice.

In the whole group, the clinical symptoms appeared at 11 ± 1,22 days, and peaked at 12,82 ± 1,42 days. At peak the averaged clinical score was of 2,56 ± 0,86 CS. The averaged weight bodies at the beginning of symptoms was 18,84 ± 2,30 g and reached the values of 16,64 ± 1,79 g at peak.

### 4.2.2. [18F]DPA-714 PET/CT uptake

The average SUV of prefrontal cortex in EAE mice was not significantly increased if compared to controls (0.227 ± 0.112 and 0.304 ± 0.139 respectively; p = 0.349). The radiotracer uptake in olfactory bulbs, cerebellum and brainstem showed a clear increase in symptomatic mice, while anterior regions of brain did not present any change (Fig. 15).

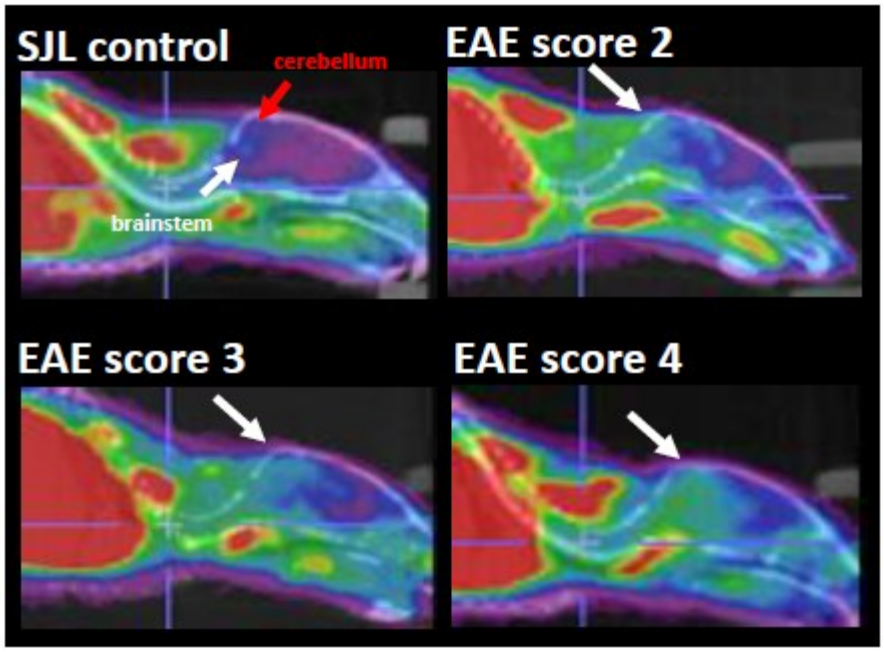


**Fig. 15** Sagittal PET images (20-50 min) co-registered to CT in EAE mice and in a control. Increased [18F]DPA-714 uptake is present in the brainstem and cerebellum. Higher uptake seems to be more marked with the increase of clinical score (CS) *(Coda et al. 2014) [95]*.

In 15 symptomatic EAE mice (clinical score range: 0.5-4), [18F]DPA-714 SUV ratios were significantly increased compared to controls in the orbitofrontal cortex (rOB: 1.408 ± 0.205 vs 1.172 ± 0.217; p = 0.022), in the cerebellum (rCBR: 1.755 ± 0.319 vs 1.321 ± 0.167; p = 0.002) and in the brainstem (rBS: 1.738 ± 0.343 and 1.359 ± 0.283; p = 0.014). Although visual assessment of PET images proved an increased [18F]DPA-714 uptake also in the upper tract of cervical spinal cord, this difference was not significant between EAE mice (2.220 ± 0.611) and control mice (1.874 ± 0.707) (p = 0.183) (Fig. 16).

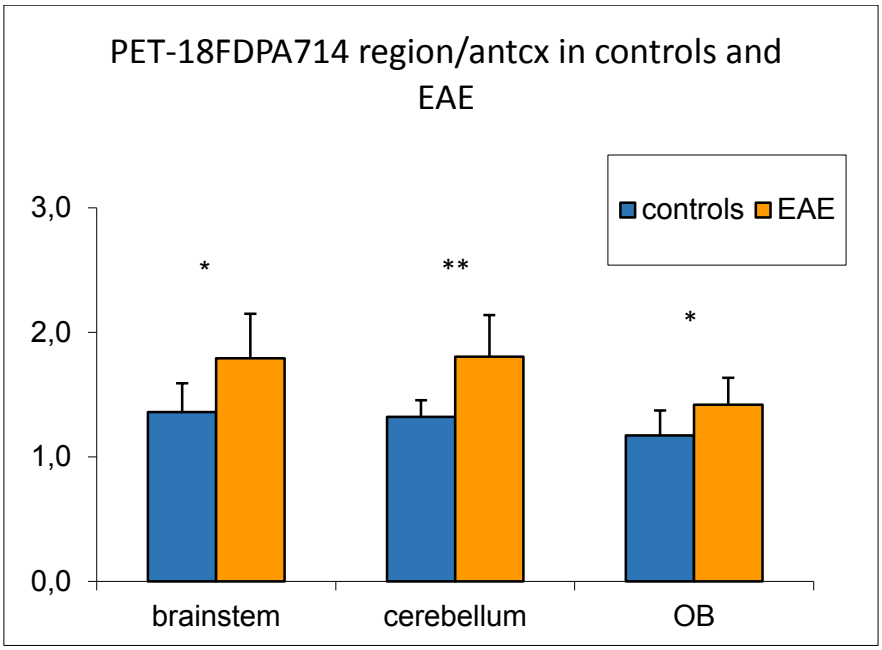


**Fig 16** On the right there are the results of PET semiquantification of [18F]DPA-714 uptake using normalization to the frontal cortex. These results show significant increase of [18F]-DPA-714 uptake in the brainstem, cerebellum and olfactory bulb in symptomatic EAE with respect to controls.

A significant positive correlation ($p<0.059$ was found between the increase of [18F]DPA-714 SUV ratios values in the cerebellum and in the brainstem and the increase of clinical score of severity.

In particular, for cerebellum the best fit linear correlation is $y=0.1407x+1.5359$ with a coefficient $R^2 = 0.2545$ (Fig. 17a) and for brainstem linear equation is $y=0.1659x+1.4798$ with a coefficient $R^2 = 0.3064$ (Fig. 17b).

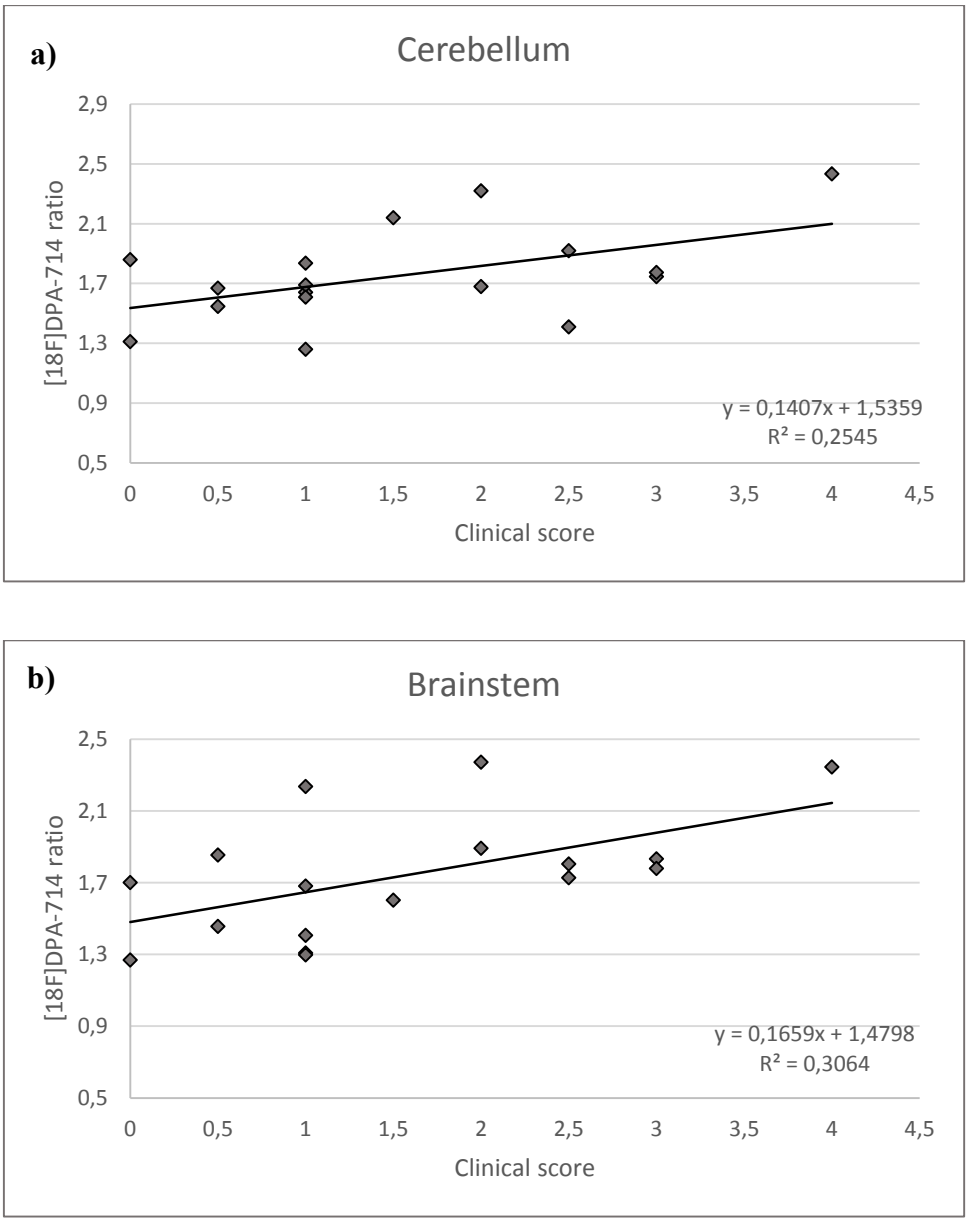


**Fig. 17** Linear correlation between [18F]DPA-714 and CS in cerebellum (a) and brainstem (b).

### 4.2.3. Immunohistochemistry

TSPO expression and microglial activation were evaluated in different areas of brain and spinal cord of symptomatic EAE and control mice underwent PET and immunofluorescence and preliminary data suggest that increased expression of TSPO in the posterior part of

brain with cerebellum and brainstem and spinal cord was significantly expressed in Iba1 positive cells. Preliminary results of double immunohistochemical analysis revealed an immunoreactivity much higher in symptomatic EAE mice, than control mice. In cerebellum, Iba1 positive cells were strongly increased in EAE mice with high CS, showing a morphological change characterized by enlargement of the cell body and shortening of cellular processes. TSPO immunoreactivity was localized mainly in Iba1 cells (Fig. 18 A). In brainstem, an abundant TSPO immunoreactivity was distribuited in Iba1 cells characterized by a larger shape, with a good colocalization with TSPO (Fig. 18 B).

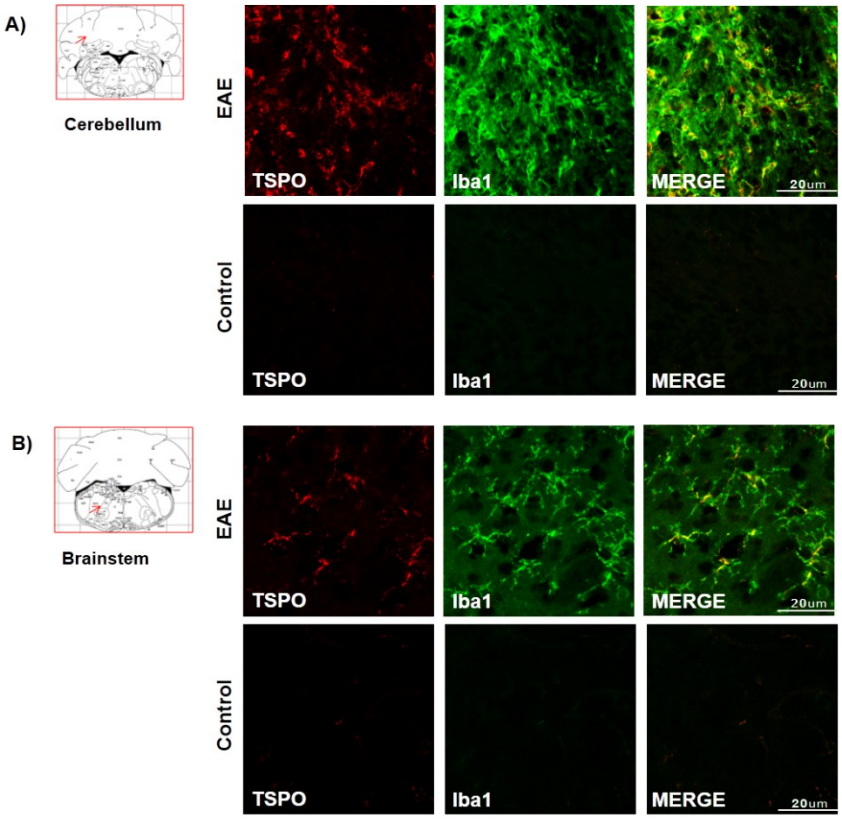


**Fig. 18** Confocal laser scanning microscopy images of TSPO and Iba1 immunofluorescence in cerebellum (A) and brainstem (B) of a symptomatic EAE mouse at CS 2.5 and a control mouse. TSPO immunolabeling (in red), Iba1 immunolabeling (in green) and merged images (in orange).

In cervical, thoracic and lumbar tract of spinal cord, Iba1 dual-label study showed an important immunolabeling increase in EAE symptomatic mice. In cervical tract Iba1 positive cells displayed a significant increase associated with an abundant TSPO immunoreactivity (Fig. 19 A). Thoracic spinal cord showed a strong increase of Iba1 immunoreactivity accompanied by a morphological change and a complete colocalization with an intense TSPO activation (Fig. 19 B). Also in lumbar tract dual-label study, TSPO immunoreactivity appeared significantly abundant and distributed principally in Iba1 cells with larger shape and shorter cellular process (Fig 19 C).

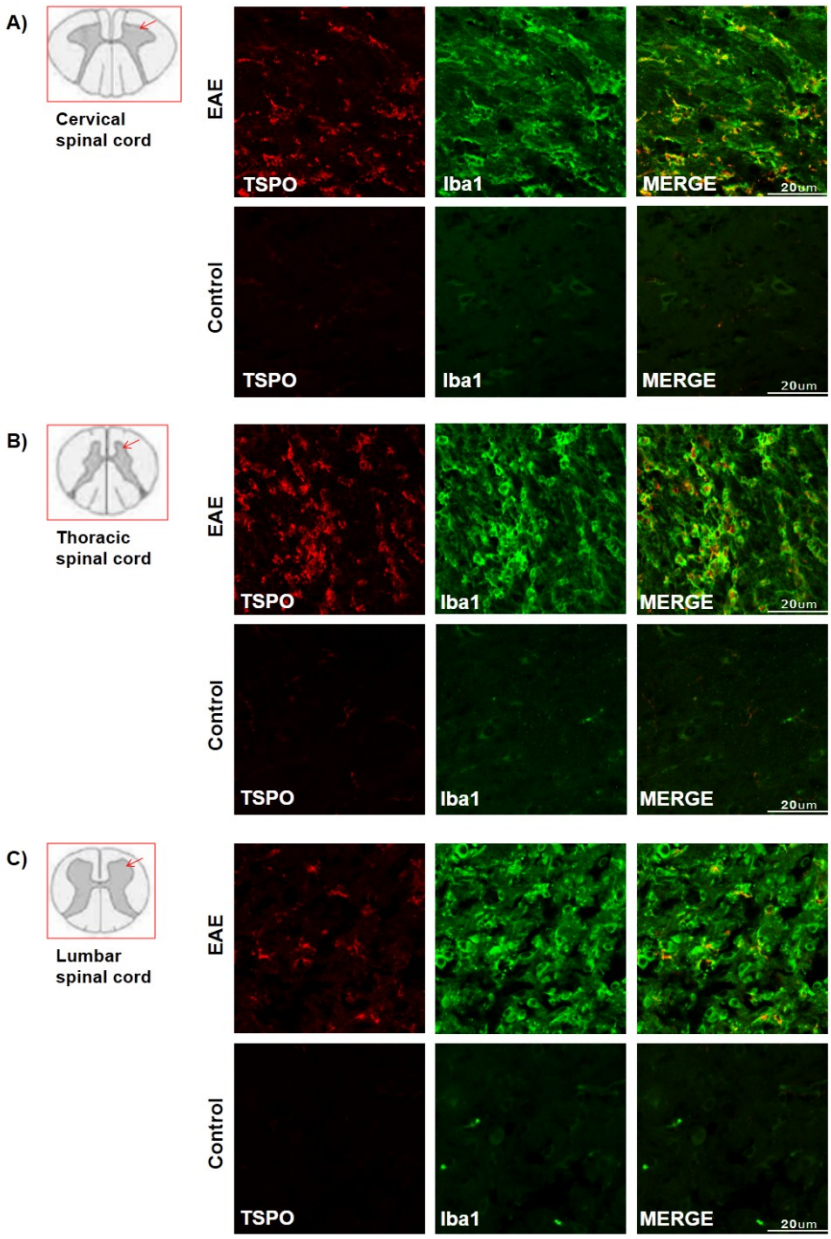


**Fig. 19** Confocal laser scanning microscopy images of TSPO and Iba1 immunofluorescence in cervical (A), thoracic (B) and lumbar (C) tract of spinal cord of a symptomatic EAE mouse at CS 2.5 and a control mouse. TSPO immunolabeling (in red), Iba1 immunolabeling (in green) and merged images (in orange).

High TSPO and Iba1 expression was found in the motor cortex and corpus callosum of two different EAE mice at CS of 3.5 and 2.5.

Striatum, hippocampus and thalamus were also observed but TSPO and microglial activation did not present. Finally, in EAE mouse at CS of 1.5, TSPO immunolabeling was very low in the different regions and some Iba1 positive cells displayed a small cell body and ramified morphology. TSPO immunoreactivity partially colocalized with microglia. In control mice, TSPO and Iba1 immunolabeling were very weakly expressed or almost completely absent in all regions examined.

## 4.3. Summary and discussion

The preliminary results of our study suggest that increased [18F]DPA-714 uptake can be measured with microPET in the olfactory bulb, in the cerebellum and in the brainstem of symptomatic mice with RR-EAE compared to controls mice. The increase of [18F]DPA-714 binding in the cerebellum and in the brainstem is related to the degree of clinical severity. In addition, the results of immunofluorescence studies revealed that in these regions there was an increase of TSPO immunolabeling that colocalized with Iba1 positive cells. Overall these results demonstrated that increased microglial activation characterizes the brain of EAE-PLP mice and can be detected in vivo with the TSPO radioligand [18F]DPA-714. These findings are in agreement with those reported in vivo with microPET using a different radioligand, the high affinity second generation TSPO radioligand [18F]PBR111, in the same EAE mouse model *[92]*. Unlike the study performed by Mattner et al. *[92]* in which the uptake of the TSPO ligand [18F]PBR111 was evaluated at different stages of disease (pre-symptomatic, first episode, second episode), we focused

our study on the characterization of TSPO changes in symptomatic mice at the first episode thus including an higher number of mice that allowed to provide more robust results. Moreover using confocal imunofluorescence we were able to characterize the expression and the colocalization of TSPO and Iba1 staining in different brain regions and in the different tracts of spinal cord. The results of our immonofluorescence studies revealed increased expression of TSPO sites in the cervical, thoracic and lumbar tracts of the spinal cord that colocalized with strongly activated microglia cells. These findings are in line with those previously reported ex-vivo and in vivo with microPET and [18F]DPA-714 in rat MBP-EAE model *[91]*. We failed, as for SOD1 G93A mice, to detect in vivo in the spinal cord significant increase in [18F]DPA-714 uptake. Partial volume effects might have reduced the accuracy in mice due to the small size of spinal cord, as discussed for SOD1 G93A mice. In addition to the cerebellum, brainstem and the spinal cord, that showed an almost constant involvement, other regions were differently affected at individual level in our mice. In particular the thalamus, the hippocampus and the striatum revealed an increased [18F]DPA-714 uptake at PET and a corresponding increased TSPO and iba1 expression in post-mortem studies. These results underlie a certain heterogeneity of NI lesions, in line with a clinical heterogeneity. Future studies in a larger number of animals will allow to better characterize the other susceptible sites of NI in EAE-PLP in vivo and ex-vivo using TSPO markers.

# 5. Conclusions and future perspectives

Overall, the results of the studies performed during this thesis suggest that TSPO sites are an interesting target for in vivo imaging of microglial activation in mice using microPET. Moreover, they highlight the feasibility of microPET studies and the relevant contribution of combined PET and immunohistochemistry for validation of new radioligands and for the characterization of cellular substrates underlying the in vivo PET signal in animal models of NI. Since PET provides also the possibility of measuring, in the same animal during the course of disease, the spatio-temporal dynamics of inflammatory cells or processes it is evident that this tool may contribute in the future to a better understanding of pathogenic mechanisms involved in animal models of NI, disease progression and therapeutic monitoring.

More in particular, the aim of this thesis was to validate a recent fluorinated PET radioligand of TSPO sites, the [18F]DPA-714. The synthesis of this radiotracer has been implemented at the Department of Advanced Biomedical Sciences, University Federico II in collaboration with the Institute of Biostructure and Bioimaging (IBB)-CNR and the PET studies were performed with the collaboration of IBB-CNR at Ceinge, Biotecnologie Avanzate thanks to the EU FP7 grant n° HEALTH-F2-2011-278850 (INMiND o Imaging of Neuroinflammation in Neurodegenerative Diseases).

In the first study, we have assessed the biodistribution and the specificity of [18F]DPA-714 in vivo in healthy mice. The results suggested that this radioligand has suitable characteristics for future in vivo studies with microPET in mice because it binds specifically to

TSPO sites, as indicated by the pattern of biodistribution and of the competitive inhibition, and it is not affected in vivo by the presence of significant radiometabolites during the time of PET studies.

Based on these positive results in healthy mice we then assessed the feasibility and sensitivity of [18F]DPA-714 in mice models of NI, combining the ex-vivo validation with immunohistochemistry.

We were the first to characterize in vivo with microPET and ex-vivo with immunolabeling the SNC patterns of microglial activation and TSPO expression in the ALS model SOD1 G93A. Despite some limitations that will be discussed below, our results demonstrated that increased TSPO expression in this mouse model could be detected in the brainstem and in the spinal cord and that it was related to increased microglial activation. Moreover, they highlight the specific neuroinflammatory involvement of brainstem nuclei and of the spinal cord in SOD1 familial form, a finding that open new perspectives in future in vivo studies of ALS patients using PET and TSPO radioligands. Interestingly, results obtained in a recent study using a multitracers PET approach, suggested that increased brain and spinal cord microglial activation measured with [11C]PK11195 in the same mouse model of ALS, might be associated with increased glutamatergic activity, measured with [18F]FPEB a specific mGluR5 radioligand *[86]*. These findings have evident therapeutic implications.

We also assessed in a third study the feasibility of microPET and [18F]DPA-714 in the study of microglial activation in the mouse model EAE-PLP. This is an acute form of MS mimicking the relapsing-remitting (RR) MS clinical form in humans. The preliminary results of these studies suggest that both brain and spinal

cord are site of increased TSPO expression in activated microglia as measured in vivo with PET and ex-vivo with immunohistochemistry. The severity of this inflammatory response seems to be related to the clinical score in the cerebellum and the brainstem, pointing out the susceptibility of these regions in this model and their role in disease severity.

Overall, our results in NI mouse models suggest that micro-PET and [18F]DPA-714 might be a useful tool for the study of microglial activation in a model of NI related to neurodegeneration such as the G93A SOD1 and in a primary acute model of NI such as the EAE-PLP.

Nevertheless, some limitations have to be considered related to the methods and to the mice animal models. The first limitation is the low spatial resolution for detecting mild changes in small structures. We failed in both SOD1 and EAE-PLP mice to detect significant radioligand increase in the spinal cord despite the ex-vivo evidence of high increased microglial activation and TSPO expression in these regions. Future studies should assess whether microPET with higher resolution, or the development of adequate methods for PVE correction, might improve the sensitivity and accuracy of the results in mice SNC models of NI. Overall, our results were obtained in a relative small number of mice, especially in the SOD1 model. Thus, further studies in a larger group of animals are needed to assess the sensitivity of [18F]DPA-714 PET in order to detect changes occurring in different regions of CNS of G93A SOD1 and EAE mice. Finally, preclinical results, although obtained in animal models showing neuropathological and clinical findings similar to those observed in humans, cannot be translated to human diseases. However they

represents an important tool for validation of new PET radioligands, characterization of the cellular substrates of in vivo PET signal, detections of PET longitudinal changes possibly including the presymptomatic stage and the evaluation of the effects of new therapeutic strategies.

# 6. Methods: radiochemistry, PET and immunohistochemistry

## 6.1. [18F]DPA-714 radiochemical synthesis

All reagents and solvents were purchased from Sigma-Aldrich Corporation. DPA-714 (N,N-diethyl-2-(2-(4-(2-fluoroethoxy)phenyl)-5,7-dimethylpyrazolo[1,5-a]pyrimidin-3-yl)acetamide) as reference compound and its tosyloxy derivative (toluene-4-sulphonicacid2-[4(3diethylcarbamoylmethyl-5,7-dimethyl-pyrazolo[1,5-a]pyrimidin-2-yl)-phenoxy]-ethyl-ester) as precursor for labeling with fluorine-18 were resynthesized in our laboratories according to previously described procedures *[96]*. No-carrier-added fluorine-18 (half-life 109.8 min) was produced via the [18O(p,n)18F] nuclear reaction by irradiation of a 2-mL [18O]water (97 % enriched; ABX, Radeberg, Germany) target on a General Electric MINItrace cyclotron (10 MeV proton beam), and the aqueous radioactive solution was then transferred to the appropriate hot cell. Target hardware consisted of a 2-mL, two-port stainless steel target holder equipped with a domed-end silver cylinder insert. The target to hot cell liquid-transfer system consisted of 33 meter tefzel tubing line (0.8 mm internal diameter; 1/16-in external diameter), 2.0 bar helium drive pressure resulting in a transfer time of 1 minute. Typical production of 18F-fluorine at the end of a 25 μAh, 60-min (12.5 μAh) irradiation was 16 – 17 GBq (732 – 769 mCi). 18F was then trapped in a Chromafix PS-HCO3 cartridge, and after elution with 0.550 mL K2CO3 (6 mg/mL) the 18F-fluorine was collected in a vessel containing Kryptofix-222 dissolved in 1 mL CH3CN (K222 15 mg/mL). [18F]DPA-714 was labeled with 18F-

fluoride starting from the corresponding precursor using a tosyloxy-for-fluorine nucleophilic aliphatic substitution according to previously described procedures with slight modification *[96-97]*. The specific activity at the end of synthesis and the radiochemical purity of [18F]DPA714 obtained within 90 min of radiosynthesis (HPLC purification and SepPak-based formulation included) were 300 GBq/μmol and N>99 %, respectively.

## 6.2. PET/CT

All the studies were performed with small animal PET/CT scanner GE Healthcare eXplore Vista (Fig. 4), designed for mice and rats. The main technical characteristics are as follows:

PET → trans-axial FOV 6.7 cm, single axial FOV 4.8 cm, spatial resolution 1.8 mm FWHM/200 μm, sensitivity 4.2% absolute central point-source sensitivity (ACS);

CT → 200 μm CT resolution, 200 μA, 35 kVp, energy windows 250–700 keV).

**Fig 20.** PET/CT scanner GE Healthcare eXplore Vista.

After the radiotracer injection, dynamic and/or static images were acquired. All the acquired PET images were reconstructed using 2D FORE/3D OSEM iterative algorithm (voxel size 0.3875×0.3875×0.775 mm) and corrected for random coincidences, scatter, physical decay to the time of injection.

Counting rates were directly converted to Standardized Uptake Values (SUV = Tissue activity (MBq/cc)/ [Injected dose (MBq)/body weight (g)]) by use of a system calibration factor (1035 Bq/mL/cps/voxel) derived from the imaging of a mouse-size water-equivalent phantom containing fluorine-18.

## 6.3. Procedures and tissue processing for immunohistochemical studies and confocal acquisition in SOD1 and EAE mice

Animals were deeply anaesthetized (isoflurane 4% and oxygen 2L/min) and transcardially perfused. They received about 30 mL ice-cold phosphate-buffered saline (0.1 M PBS), followed by about 60 mL of 4 % paraformaldehyde in saline solution. The brains and spinal cords were isolated, postfixed overnight at 4°C in 4% paraformaldehyde and cryoprotected in 30% sucrose in 0.1 M PBS for 48h at 4°C. Sections were obtained using a sliding cryostat at 40 μm thickness. In collaboration with the Department of Neuroscience, Reproductive and Dentistry Sciences of University of Naples "Federico II", free-floating sections were subjected to immunostaining and were incubated first with blocking solution (0.5% milk, 10% fetal bovine serum, 1 % bovine serum albumin) for 1.30h. Then, section were incubated overnight at 4°C with the following primary antibodies: rabbit monoclonal anti-PBR (1:500; Novus Biologicals) and mouse monoclonal anti-Iba1 (ionized calcium binding adapter molecule 1, 1:1000; Abcam). IBA1 is a 17-kDa EF hand protein that is specifically expressed in macrophages/microglia and is upregulated during the activation of these cells *[98]*, following nerve injury, central nervous system ischemia, and several other brain diseases *[99]*. The sections were subsequently incubated with a cocktail of the corresponding fluorescent-labeled secondary antibodies (Alexa 488/Alexa 594-conjugated antimouse/antirabbit IgGs).

In double-labeled sections, the pattern of immunoreactivity for both antigens was identical to that seen in single-stained material. Control

double immunofluorescence staining entailed the replacement of the primary antisera with normal serum (data not shown). To minimize possible crossreactivity between IgGs in double immunolabeling experiments, the full complement of secondary antibodies was maintained, but the primary antisera were replaced with normal serum or only one primary antibody was applied (data not shown). In addition, the secondary antibodies were highly preadsorbed to the IgGs of numerous species. Tissue labeling without primary antibodies was also tested to exclude autofluorescence. No specific staining was observed under these control conditions, thus confirming the specificity of the immunosignals.

Images were observed using a confocal microscope Zeiss LSM 700 (Fig. 21). It is a four laser, point scanning confocal with a single pinhole and works together with ZEN software to obtain final images.

Confocal microscopy is an optical imaging technique able to reconstruct a three-dimensional structure from sets of images obtained at different depths thanks to the use of a pinhole placed at the confocal plane of the lens to eliminate out-of-focus light. Fluorescence emission passing through the pinhole is reflected onto the diffraction grating surface using a dichromatic mirror. The spectrally separated light is then projected through the slit and into the photomultiplier.


**Fig 21.** Confocal microscope Zeiss LSM 700

Single images were taken with an optical thickness of 0.7 μm at a resolution of 1024×1024 and 40× magnification.

## Fundings

All experiments of this project were funded by the European Union's Seventh Framework Programme (FP7/2007-2013) under grant agreement no. HEALTH-FP-2011-278850 (INMIND).

# Bibliography


1. Graeber MB, Li W, Rodriguez ML. Role of microglia in CNS inflammation. FEBS Lett. 2011; 585(23):3798-805.
2. Jacobs AH, Tavitian B; INMiND consortium. Noninvasive molecular imaging of neuroinflammation. J Cereb Blood Flow Metab. 2012; 32(7):1393-415.
3. Ory D, Celen S, Verbruggen A, Bormans G. PET Radioligands for In Vivo Visualization of Neuroinflammation. Curr Pharm Des. 2014; 20:5897-5913.
4. Lucas SM, Rothwell NJ, Gibson RM. The role of inflammation in CNS injury and disease. Br J Pharmacol. 2006; 147: 232-40.
5. Glass CK, Saijo K, Winner B, Marchetto MC, Gage FH. Mechanisms underlying inflammation in neurodegeneration. Cell 2010; 140: 918-934.
6. Dantzer R, Konsman JP, Bluthe RM, Kelley KW. Neural and humoral pathways of communication from the immune system to the brain: parallel or convergent? Auton Neurosci 2000; 85:60–65.
7. Besedovsky HO, Rey AD. Physiology of psychoneuroimmunology: a personal view. Brain Behav Immun 2007; 21:34–44.
8. Teeling JL, Perry VH. Systemic infection and inflammation in acute CNS injury and chronic neurodegeneration: underlying mechanisms. Neuroscience. 2009; 158(3):1062-73.

9. Banks WA. Blood-brain barrier transport of cytokines: a mechanism for neuropathology. Curr Pharm Des. 2005; 11(8):973-84.
10. Turrin NP, Rivest S. Unraveling the molecular details involved in the intimate link between the immune and neuroendocrine systems. Exp Biol Med (Maywood). 2004; 229(10):996-1006.
11. Airas L, Dickens AM, Elo P, Marjamäki P, Johansson J, Eskola O, *et al*. In vivo PET imaging demonstrates diminished microglial activation after fingolimod treatment in an animal model of multiple sclerosis. J Nucl Med. 2015; 56(2):305-10.
12. Garden GA, Möller T. Microglia biology in health and disease. J Neuroimmune Pharmacol. 2006; 1(2):127-37.
13. Czeh M, Gressens P, Kaindl AM. The yin and yang of microglia. Dev Neurosci. 2011; 33(3-4):199-209.
14. Wunder A, Klohs J, Dirnagl U. Non-invasive visualization of CNS inflammation with nuclear and optical imaging. Neuroscience 2009; 158:1161-1173.
15. Waerzeggers Y, Monfared P, Viel T, Winkeler A, Jacobs AH. Mouse models in neurological disorders: applications of non-invasive imaging. Biochim Biophys Acta 2010; 1802:819-839.
16. Schwab C, Klegeris A, McGeer PL. Inflammation in transgenic mouse models of neurodegenerative disorders. Biochimica et Biophysica Acta 2010; 1802(10):889-902.
17. Kiernan MC, Vucic S, Cheah BC, Turner MR, Eisen A, Hardiman O, et al. Amyotrophic lateral sclerosis. Lancet. 2011; 377:942–55.
18. Zinman L, Cudkowicz M. Emerging targets and treatments in amyotrophic lateral sclerosis. Lancet Neurol 2011; 10:481-490.

19. McGoldrick P, Joyce PI, Fisher EMC, Greensmith L. Rodent models of amyotrophic lateral sclerosis. Biochimica et Biophysica Acta 2013; 1832(9):1421–36.
20. Cleveland DW, Rothstein JD. From Charcot to Lou Gehrig: deciphering selective motor neuron death in ALS. Nat Rev Neurosci. 2001; 2(11):806-19.
21. Shibata N, Hirano A, Yamamoto T, Kato Y, Kobayashi M. Superoxide dismutase-1 mutation-related neurotoxicity in familial amyotrophic lateral sclerosis. Amyotroph Lateral Scler Other Motor Neuron Disord. 2000; 1(3):143-61.
22. Rosen DR, Siddique T, Patterson D, et al. Mutations in Cu/Zn superoxide dismutase gene are associated with familial amyotrophic lateral sclerosis. Nature 1993; 362:59-62.
23. Shibata N. Transgenic mouse model for familial amyotrophic lateral sclerosis with superoxide dismutase-1 mutation. Neuropathology. 2001; 21(1):82-92.
24. Gurney ME, Pu H, Chiu AY, et al. Motor neuron degeneration in mice that express a human Cu,Zn superoxide dismutase mutation. Science 1994; 264:1772-1775.
25. Wong PC, Pardo CA, Borchelt DR, Lee MK, Copeland NG, Jenkins NA, Sisodia SS, Cleveland DW, Price DL. An adverse property of a familial ALS-linked SOD1 mutation causes motor neuron disease characterized by vacuolar degeneration of mitochondria. Neuron. 1995; 14(6):1105-16.
26. Hooten KG, Beers DR, Zhao W, Appel SH. Protective and Toxic Neuroinflammation in Amyotrophic Lateral Sclerosis. Neurotherapeutics. 2015; 12(2):364-75.

27. Philips T, Robberecht W. Neuroinflammation in amyotrophic lateral sclerosis: role of glial activation in motor neuron disease. Lancet Neurol. 2011; 10(3):253-63.
28. Evans MC, Couch Y, Sibson N, Turner MR. Inflammation and neurovascular changes in amyotrophic lateral sclerosis. Mol Cell Neurosci. 2013; 53:34-41.
29. Ferrucci M, Spalloni A, Bartalucci A, Cantafora E, Fulceri F, Nutini M, Longone P, Paparelli A, Fornai F. A systematic study of brainstem motor nuclei in a mouse model of ALS, the effects of lithium. Neurobiol Dis. 2010; 37(2):370-83.
30. Calabrese M, Magliozzi R, Ciccarelli O, Geurts JJ, Reynolds R, Martin R. Exploring the origins of grey matter damage in multiple sclerosis. Nat Rev Neurosci 2015; 16: 147-58.
31. Peferoen LA, Vogel DY, Ummenthum K, Breur M, Heijnen PD, Gerritsen WH, Peferoen-Baert RM, van der Valk P, Dijkstra CD, Amor S. Activation status of human microglia is dependent on lesion formation stage and remyelination in multiple sclerosis. J Neuropathol Exp Neurol. 2015; 74(1):48-63.
32. Nylander A and Hafler DA. Multiple sclerosis. J Clin Invest 2012; 122:1180-8.
33. De Paula Faria D, Copray S, Buchpiguel C, Dierckx R, de Vries E. PET imaging in multiple sclerosis. J Neuroimmune Pharmacol. 2014; 9(4):468-82.
34. Pittock SJ, Lucchinetti CF. The pathology of MS. New insights and potential clinical applications. The Neurologist. 2007; 13:45-56.

35. Popescu BFG, Lucchinetti CF. Pathology of demeylinating diseases. Annu Rev Pathol Mech Dis. 2012; 7:185-217.
36. Gold R, Linington C and Lassmann H. Understanding pathogenesis and therapy of multiple sclerosis via animal models: 70 years of merits and culprits in experimental autoimmune encephalomyelitis research. Brain. 2006; 129(Pt 8):1953-71.
37. Koritschoner RS, Schweinburg F. Induktion von Paralyse und Ruckenmarksentzundung durch Immunisierung von Kaninchen mit menschlichem Ruckenmarksgewebe. Z Immunitatsf Exp Therapie 1925; 42: 217–83.
38. Rivers TM, Sprunt DH, Berry GP. Observation on attempts to produce acute disseminated encephalomyelitis in monkeys. J Exp Med. 1933; 58(1):39-53.
39. Kabat EA, Wolf A, Bezer AE. The rapid production of acute disseminated encephalomyelitis in rhesus monkeys by injection of heterologous and homologous brain tissue with adjuvants. J Exp Med. 1947; 85(1):117-30.
40. Munoz JJ, Bernard CC, Mackay IR. Elicitation of experimental allergic encephalomyelitis (EAE) in mice with the aid of pertussigen. Cell Immunol. 1984; 83(1):92-100.
41. Procaccini C, De Rosa V, Pucino V, Formisano L, Matarese G. Animal models of Multiple Sclerosis. Eur J Pharmacol 2015; 759:182-91.
42. Airas L, Rissanen E, Rinne JO. Imaging neuroinflammation in multiple sclerosis using TSPO-PET. Clin Transl Imaging. 2015; 3:461-473.

43. Schreiner B, Heppner FL, Becher B. Modeling multiple sclerosis in laboratory animals. Semin Immunopathol. 2009; 31:479–495.
44. Teuscher C, Bunn JY, Fillmore PD, Butterfield RJ, Zachary JF, Blankenhorn EP. Gender, age, and season at immunization uniquely influence the genetic control of susceptibility to histopathological lesions and clinical signs of experimental allergic encephalomyelitis: implications for the genetics of multiple sclerosis. Am J Pathol 2004; 165:1593–1602.
45. Fillmore PD, Brace M, Troutman SA, Blankenhorn EP, Diehl S, Rincon M et al. Genetic analysis of the influence of neuroantigen-complete Freund's adjuvant emulsion structures on the sexual dimorphism and susceptibility to experimental allergic encephalomyelitis. Am J Pathol. 2003; 163(4):1623-32.
46. Oliver AR, Lyon GM, Ruddle NH. Rat and human myelin oligodendrocyte glycoproteins induce experimental autoimmune encephalomyelitis by different mechanisms in C57BL/6 mice. J Immunol. 2003; 171(1):462-8.
47. Papadopoulos V, Baraldi M, Guilarte TR, Knudsen TB, Lacapère JJ, Lindemann P, Norenberg MD, Nutt D, Weizman A, Zhang MR, Gavish M. Translocator protein (18kDa): new nomenclature for the peripheral-type benzodiazepine receptor based on its structure and molecular function. Trends Pharmacol Sci. 2006; 27(8):402-9.
48. Chen MK, Guilarte TR. Translocator protein 18 kDa (TSPO): molecular sensor of brain injury and repair. Pharmacol Ther. 2008; 118(1):1-17.

49. Gavish M, Bachman I, Shoukrun R, Katz Y, Veenman L, Weisinger G, Weizman A. Enigma of the peripheral benzodiazepine receptor. Pharmacol Rev. 1999;51(4):629-50.
50. Papadopoulos V, Lecanu L. Translocator protein (18kDa) TSPO: an emerging therapeutic target in neurotrauma. Exp Neurol. 2009; 219: 53-57.
51. Banati RB. Visualising microglial activation in vivo. Glia. 2002; 40(2):206-17.
52. Rupprecht R, Papadopoulos V, Rammes G, Baghai TC, Fan J, Akula N, *et al*. Translocator protein (18 kDa) (TSPO) as a therapeutic target for neurological and psychiatric disorders. Nat Rev Drug Discov 2010; 9: 971-88.
53. Venneti S, Lopresti BJ, Wiley CA. Molecular imaging of microglia/macrophages in the brain. Glia. 2013; 61(1):10-23.
54. Phelps ME. Positron emission tomography provides molecular imaging of biological processes. Proc Natl Acad Sci U S A. 2000; 97(16):9226-33.
55. Camsonne R, Crouzel C, Comar D, Mazière M, Prenant C, Sastre J, Moulin M and Syrota A. Synthesis of N-(11C) methyl, N-(methyl-1 propyl), (chloro-2 phenyl)-1 isoquinoleine carboxamide-3 (PK 11195): a new ligand for peripheral benzodiazepine receptors. Journal of Labelled Compounds and Radiopharmaceuticals 1984; 21:985-991.
56. Ching AS, Kuhnast B, Damont A, Roeda D, Tavitian B, Dollé F. Current paradigm of the 18-kDa translocator protein (TSPO) as a molecular target for PET imaging in neuroinflammation and neurodegenerative diseases. Insights Imaging. 2012; 3(1):111-9.

57. Chauveau F, Boutin H, Van Camp N, Dollé F, Tavitian B. Nuclear imaging of neuroinflammation: a comprehensive review of [11C]PK11195 challengers. Eur J Nucl Med Mol Imaging. 2008; 35(12):2304-19.
58. Lockhart A, Davis B, Matthews JC, et al. The peripheral benzodiazepine receptor ligand PK11195 binds with high affinity to the acute phase reactant α1-acid glycoprotein: implications for the use of the ligand as a CNS inflammatory marker. Nucl Med Biol. 2003; 30: 199–206.
59. James ML, Fulton RR, Vercoullie J, Henderson DJ, Garreau L, Chalon S, Dolle F, Costa B, Guilloteau D, Kassiou M. DPA-714, a new translocator protein-specific ligand: synthesis, radiofluorination, and pharmacologic characterization. J Nucl Med. 2008; 49(5):814-22.
60. James M, Fulton R, Henderson D, et al. Synthesis and in vivo evaluation of a novel peripheral benzodiazepine receptor PET radioligand. Bioorg Med Chem. 2005; 13:6188–6194.
61. Chauveau F, Van Camp N, Dollé F, Kuhnast B, Hinnen F, Damont A, Boutin H, James M, Kassiou M, Tavitian B. Comparative evaluation of the translocator protein radioligands 11C-DPA-713, 18F-DPA-714, and 11C-PK11195 in a rat model of acute neuroinflammation. J Nucl Med. 2009; 50(3):468-76.
62. Doorduin J, Vellinga NAR, Klein HC, Kassiou M, James M, Dierckx RA, et al. PET imaging of neuroinflammation in a rat model of herpes encephalitis: a comparison of [11C]-(R)-PK11195 and [11C]-DPA-713. Eur J Nucl Med Mol Imaging. 2006; 33:S192.

63. Martin A, Boisgard R, Theze B, Van Camp N, Kuhnast B, Damont A, et al. Evaluation of the PBR/TSPO radioligand [(18)F]DPA-714 in a rat model of focal cerebral ischemia. J Cereb Blood Flow Metab 2010; 30:230–41.
64. Arlicot N, Vercouillie J, Ribeiro MJ, Tauber C, Venel Y, Baulieu JL, et al. Initial evaluation in healthy humans of [18 F]DPA-714, a potential PET biomarker for neuroinflammation. Nucl Med Biol 2012; 39:570–8.
65. Peyronneau MA, Saba W, Goutal S, Damont A, Dolle F, Kassiou M, et al. Metabolism and quantification of [(18)F]DPA-714, a new TSPO positron emission tomography radioligand. Drug Metab Dispos 2013; 41:122–31.
66. Boutin H, Prenant C, Maroy R, Galea J, Greenhalgh AD, Smigova A, et al. [18 F]DPA-714: direct comparison with [11C]PK11195 in a model of cerebral ischemia in rats. PLoS One 2013; 8:e56441.
67. Zinnhardt B, Viel T, Wachsmuth L, Vrachimis A, Wagner S, Breyholz HJ, Faust A, Hermann S, Kopka K, Faber C, Dollé F, Pappata S, Planas AM, Tavitian B, Schäfers M, Sorokin LM, Kuhlmann MT, Jacobs AH. Multimodal imaging reveals temporal and spatial microglia and matrix metalloproteinase activity after experimental stroke. J Cereb Blood Flow Metab. 2015; 35(11):1711-21.
68. Vicidomini C, Panico M, Greco A, Gargiulo S, Coda AR, Zannetti A, *et al*. In vivo imaging and characterization of [$^{18}$F]DPA-714, a potential new TSPO ligand, in mouse brain and peripheral tissues using small-animal PET. Nucl Med Biol 2015; 42: 309-16.

69. Yanamoto K, Kumata K, Fujinaga M, Nengaki N, Takei M, Wakizaka H, et al. In vivo imaging and quantitative analysis of TSPO in rat peripheral tissues using small animal PET with [18 F]FEDAC. Nucl Med Biol 2010; 37:853–60.
70. Hashimoto K, Inoue O, Suzuki K, Yamasaki T, Kojima M. Synthesis and evaluation of 11C-PK 11195 for in vivo study of peripheral-type benzodiazepine receptors using positron emission tomography. Ann Nucl Med 1989; 3:63–71.
71. Turner MR, Cagnin A, Turkheimer FE, Miller CC, Shaw CE, Brooks DJ, et al. Evidence of widespread cerebral microglial activation in amyotrophic lateral sclerosis: an [11C](R)-PK11195 positron emission tomography study. Neurobiol Dis. 2004; 15:601–9.
72. Corcia P, Tauber C, Vercoullie J, Arlicot N, Prunier C, Praline J, et al. Molecular imaging of microglial activation in amyotrophic lateral sclerosis. PLoS One. 2012; 7:e52941.
73. Zürcher NR, Loggia ML, Lawson R, Chonde DB, Izquierdo-Garcia D, Yasek JE, Akeju O, Catana C, Rosen BR, Cudkowicz ME, Hooker JM, Atassi N. Increased in vivo glial activation in patients with amyotrophic lateral sclerosis: assessed with [(11)C]-PBR28. Neuroimage Clin. 2015; 7:409-14.
74. Venneti S, Wang G, Nguyen J, Wiley CA. The positron emission tomography ligand DAA1106 binds with high affinity to activated microglia in human neurological disorders. J Neuropathol Exp Neurol. 2008; 67:1001–10.
75. Solomon JA, Tarnopolsky MA, Hamadeh MJ. One universal common endpoint in mouse models of amyotrophic lateral sclerosis. PLoS One 2011; 6(6):e20582.

76. Ludolph AC, Bendotti C, Blaugrund E, Chio A, Greensmith L, Loeffler JP, Mead R, Niessen HG, Petri S, Pradat PF, Robberecht W, Ruegg M, Schwalenstöcker B, Stiller D, van den Berg L, Vieira F, von Horsten S. Guidelines for preclinical animal research in ALS/MND: A consensus meeting. Amyotroph Lateral Scler. 2010; 11: 38-45.
77. Paxinos G, Franklin KB. The mouse brain in stereotaxic coordinates. San Diego: Elsevier Academic Press; 2001.
78. Leichsenring A, Linnartz B, Zhu XR, Lubbert H, Stichel CC. Ascending neuropathology in the CNS of a mutant SOD1 mouse model of amyotrophic lateral sclerosis. Brain Res. 2006; 1096: 180– 95.
79. Bucher S, Braunstein KE, Niessen HG, Kaulisch T, Neumaier M, Boeckers TM, et al. Vacuolization correlates with spin-spin relaxation time in motor brainstem nuclei and behavioural tests in the transgenic G93A-SOD1 mouse model of ALS. Eur J Neurosci. 2007; 26:1895–901.
80. Zang DW, Yang Q, Wang HX, Egan G, Lopes EC, Cheema SS. Magnetic resonance imaging reveals neuronal degeneration in the brainstem of the superoxide dismutase 1 transgenic mouse model of amyotrophic lateral sclerosis. Eur J Neurosci. 2004; 20:1745–51.
81. Chung YH, Joo KM, Lee YJ, Shin DH, Cha CI. Reactive astrocytes express PARP in the central nervous system of SOD(G93A) transgenic mice. Brain Res. 2004; 1003:199–204.
82. Ozdinler PH, Benn S, Yamamoto TH, Güzel M, Brown Jr RH, Macklis JD. Corticospinal motor neurons and related subcerebral projection neurons undergo early and specific

neurodegeneration in hSOD1G93A transgenic ALS mice. J Neurosci. 2011; 31:4166-77.

83. Zang DW, Cheema SS. Degeneration of corticospinal and bulbospinal systems in the superoxide dismutase 1(G93A G1H) transgenic mouse model of familial amyotrophic lateral sclerosis. Neurosci Lett. 2002; 332:99–102.
84. Hall ED, Oostveen JA, Gurney ME. Relationship of microglial and astrocytic activation to disease onset and progression in a transgenic model of familial ALS. Glia. 1998; 23:249–56.
85. Alexianu ME, Kozovska M, Appel SH. Immune reactivity in a mouse model of familial ALS correlates with disease progression. Neurology. 2001; 57:1282–9.
86. Brownell AL, Kuruppu D, Kil KE, Jokivarsi K, Poutiainen P, Zhu A, et al. PET imaging studies show enhanced expression of mGluR5 and inflammatory response during progressive degeneration in ALS mouse model expressing SOD1-G93A gene. J Neuroinflammation. 2015; 12:217.
87. Gargiulo S, Anzilotti S, Coda AR, Gramanzini M, Greco A, Panico M, et al. Imaging of brain TSPO expression in a mouse model of amyotrophic lateral sclerosis with 18F-DPA-714 and micro-PET/CT. Eur J Nucl Med Mol Imaging 2016; 43: 1348-1359.
88. Gargiulo S, Coda AR, Panico M, Gramanzini M, Moresco RM, Chalon S, Pappatà S. Molecular imaging of neuroinflammation in preclinical rodent models using positron emission tomography. Q J Nucl Med Mol Imaging. 2017; 61(1):60-75.
89. Radu CG, Shu CJ, Shelly SM, Phelps ME, Witte ON. Positron emission tomography with computed tomography imaging of

neuroinflammation in experimental autoimmune encephalomyelitis. Proc Natl Acad Sci U S A. 2007; 104(6):1937-42.

90. Buck D, Förschler A, Lapa C, Schuster T, Vollmar P, Korn T, *et al.* 18F-FDG PET detects inflammatory infiltrates in spinal cord experimental autoimmune encephalomyelitis lesions. J Nucl Med. 2012; 53(8):1269-76.
91. Abourbeh G, Thézé B, Maroy R, Dubois A, Brulon V, Fontyn Y, Dollé F, Tavitian B, Boisgard R. Imaging microglial/macrophage activation in spinal cords of experimental autoimmune encephalomyelitis rats by positron emission tomography using the mitochondrial 18 kDa translocator protein radioligand [$^{18}$F]DPA-714. J Neurosci. 2012; 32(17):5728-36.
92. Mattner F, Staykova M, Berghofer P, Wong HJ, Fordham S, Callaghan P, Jackson T, Pham T, Gregoire MC, Zahra D, Rahardjo G, Linares D, Katsifis A. Central nervous system expression and PET imaging of the translocator protein in relapsing-remitting experimental autoimmune encephalomyelitis. J Nucl Med. 2013; 54(2):291-8.
93. De Rosa V, Procaccini C, La Cava A, Chieffi P, Nicoletti GF, Fontana S, Zappacosta S, Matarese G. Leptin neutralization interferes with pathogenic T cell autoreactivity in autoimmune encephalomyelitis.J Clin Invest. 2006; 116(2):447-55.
94. Gelderblom M, Daehn T, Schattling B, Ludewig P, Bernreuther C, Arunachalam P, Matschke J, Glatzel M, Gerloff C, Friese MA, Magnus T. Plasma levels of neuron specific enolase quantify the extent of neuronal injury in murine models of

ischemic stroke and multiple sclerosis. Neurobiol Dis. 2013; 59:177-82.

95. Coda AR, Greco A, Zannetti A, Barba P, Vicidomini C, Panico MR, Albanese S, Azillotti S, Gargiulo S, Gramanzini M, Dollé F, de Berardinis P and Pappatà S. PET Imaging of brain TSPO expression in a mouse model of Experimental Autoimmune Encephalomyelitis using [18F]DPA-714. European Journal of Nuclear Medicine and Molecular Imaging 2014; 41(2):S322-S323.
96. Damont A, Hinnen F, Kuhnast B, Schöllhorn-Peyronneau M-A, James M, Luus C, et al. Radiosynthesis of [18F]DPA-714, a selective radioligand for imaging the translocator protein (18 kDa) with PET. J Label Comp Radiopharm. 2008; 51:286–92.
97. Kuhnast B, Damont A, Hinnen F, Catarina T, Demphel S, Le Helleix S, et al. [18F]DPA-714, [18F]PBR111 and [18F]FEDAA1106-selective radioligands for imaging TSPO 18 kDa with PET: automated radiosynthesis on a TRACERLAb FXFN synthesizer and quality controls. Appl Radiat Isot. 2012; 70:489–97.
98. Sasaki Y, Ohsawa K, Kanazawa H, Kohsaka S, Imai Y. Iba1 is an actin-cross-linking protein in macrophages/microglia. Biochem Biophys Res Commun. 2001; 286(2):292-7.
99. Ito D, Imai Y, Ohsawa K, Nakajima K, Fukuuchi Y, Kohsaka S. Microglia-specific localisation of a novel calcium binding protein, Iba1. Brain Res Mol Brain Res. 1998; 57(1):1-9.